AGU
PUBLICATIONS

1 **On the relation between seismic source dynamics, tsunami**
2 **generation and propagation, and numerical modelling**
3 **complexity for large earthquakes in subduction zones**

4

5 **A. Scala[1,2], S. Lorito[2], C. Escalante Sánchez[3], F. Romano[2], G. Festa[1,2], A. Abbate[2,4], H. B.**
6 **Bayraktar[2], M. J. Castro[3], J. Macías[3], J. M. Gonzalez-Vida[3]**

7

8 [1] Department of Physics "Ettore Pancini", University Federico II, Napoli, 80126, Italy.

9 [2] Istituto Nazionale di Geofisica e Vulcanologia, Rome, 00143, Italy

10 [3] EDANYA Group, University of Malaga, Malaga, 29080, Spain

11 [4] Department of Mathematics, Informatics and Geosciences, University of Trieste, 34128, Italy

12

13 Corresponding author: Antonio Scala (antonio.scala@unina.it)

14

15 **Key Points:**

16 • Slow and large ruptures (e.g. tsunami earthquakes and mega-thrust) require a time-
17 dependent, non-hydrostatic modelling

18 • Deeper, high stress-drop earthquakes might be modelled through an instantaneous source,
19 shallow water approximation

20 • Inundation depends on bathymetric features: larger inundations on steeper depth gradients
21 and resonant run-up amplifications are observed

22
23

24 **Abstract**

25 Tsunamis are rare, destructive events, whose generation, propagation and coastal impact processes
26 involve several complex physical phenomena. Most tsunami applications, like probabilistic
27 tsunami hazard assessment, make extensive use of large sets of numerical simulations, facing a
28 systematic trade-off between the computational costs and the modelling accuracy. For seismogenic
29 tsunami, the source is often modelled as an instantaneous sea-floor displacement due to the fault
30 static slip distribution, while the propagation in open-sea is computed through a shallow water
31 approximation.
32 Here, through 1D earthquake-tsunami coupled simulations of large M>8 earthquakes in Tohoku-
33 like subduction zone, we tested for which conditions the instantaneous source (IS) and/or the
34 shallow water (SW) approximations can be used to simulate with enough accuracy the whole
35 tsunami evolution. We used as a reference a time-dependent (TD), multi-layer, non-hydrostatic
36 (NH) model whose source features, duration, and size, are based on seismic rupture dynamic
37 simulations with realistic stress drop and rigidity, within a Tohoku-like environment.
38 We showed that slow ruptures, generating slip in shallow part of subduction slabs (e.g. tsunami
39 earthquakes), and very large events, with an along-dip extension comparable with the trench-coast
40 distance (e.g. mega-thrust) require a TD-NH modelling, in particular when the bathymetry close
41 to the coast features sharp depth gradients. Conversely, deeper, higher stress-drop events can be
42 accurately modelled through an IS-SW approximation. We finally showed to what extent
43 inundation depend on bathymetric geometrical features: (i) steeper bathymetries generate larger
44 inundations and (ii) a resonant mechanism emerges with run-up amplifications associated with
45 larger source size on flatter bathymetries.
46

47 **Plain Language Summary**

48 In the last two decades, tsunamis originated by large earthquakes have generated major damages
49 and more than 250k casualties. Strategies to quantify and mitigate the associated risk are based on
50 numerical simulations of the physical processes regulating the generation, propagation of the
51 waves and subsequent flooding on the coast. These simulations would require unaffordable
52 computational resources; to solve this problem, numerous approximations are introduced that need
53 to be tested. In this work, we studied which earthquakes, depending on the speed at which they
54 deform the sea bottom when they trigger a tsunami, and on how big they are, require a more
55 detailed modelling approach, and which ones, instead, might be accurately simulated through
56 approximated approaches. We also show how such findings are related to different bathymetric
57 characteristics near the coast and inland, which may enhance or reduce the tsunami effects.

58

59 **1 Introduction**

60 Due to the rare occurrence of tsunamis and the strong influence of bathymetry and coastal
61 morphology on tsunami evolution, tsunami community makes use of numerical simulations to
62 compensate for the scarcity of observations (see e.g. Behrens et al., 2021; Sugawara, 2021;
63 Babeyko et al., 2022). Here, we consider tsunamis generated by earthquakes in subduction zones,
64 since the most destructive tsunamis in the last decades were generated by interslab subduction
65 events (Grezio et al., 2017; Davies & Griffin, 2020). For these sources, tsunami simulations require
66 the numerical modelling of the earthquake source process, the solid-fluid interaction during the

67 tsunami generation, and the wave propagation on a complex bathymetry up to the inundation of
68 the coastal topography. Numerical modelling of these diverse physical processes typically requires
69 different solvers with a certain level of coupling between them. They range from the simplest
70 solution consisting of instantaneous seafloor from a static slip (Okada, 1985) to more complex
71 modelling implementing either a two-step (Saito et al., 2019) or a fully coupled approach to
72 describe the seismic and the tsunami source processes (Lotto & Dunham, 2015; Lotto et al., 2019).
73
74 Each solver adopts approximations and simplifications to limit the computational cost associated
75 with the simulations. This is particularly relevant when an application requires many high-
76 resolution simulations, such as in probabilistic tsunami hazard analysis (PTHA, Grezio et al., 2017;
77 Davies et al., 2018; Gibbons et al., 2020; Basili et al., 2021; Behrens et al., 2021), inverse problems
78 (Romano et al., 2020, 2021), or tsunami forecasting for early warning purposes (Selva et al., 2021).
79 One way to cope with the containment of the computational cost is to approximate the tsunami
80 height after shoaling, or the runup process with analytical or stochastic methods (Brocchini &
81 Peregrine, 1996; Gailler et al., 2018; Glimsdal et al., 2019; Souty & Gailler, 2021). Recently, an
82 emerging way to approach the problem is to exploit emulators as surrogates of the simulations
83 (Gopinathan et al., 2021; Ehara et al., 2023) or AI-based techniques to estimate the inundation
84 parameters from offshore or low-resolution simulations (Makinoshima et al., 2021; Ehara et al.,
85 2023). From a distinct perspective, the computational cost of numerical modeling can be reduced
86 without losing resolution by opportunely decreasing the number of simulations. This can be done
87 by performing an optimal sampling of the parameter space (e.g. Davies et al., 2022), or by
88 exploiting the similarity of tsunami scenarios due to different earthquake sources (e.g. Williamson
89 et al., 2020).
90 All these strategies are complementary to the purpose of this study, which aims to establish an
91 optimal simulation strategy for the specific case of large earthquakes in subduction zones and the
92 ensuing tsunamis.
93
94 The subduction slab is often represented as a planar or a segmented interface (LeVeque et al.,
95 2016; Li et al., 2016; Sepúlveda et al., 2017). However, recently, curved surfaces are being
96 modelled increasingly often (Nakano et al., 2020; Scala et al., 2020; Tonini et al., 2020). The
97 seismic rupture on the interface is modelled as an instantaneous elastic dislocation, or as the linear
98 superposition of dislocations of different amplitude representing heterogeneous slip distributions,
99 in a homogeneous half-space (Okada, 1985; Meade, 2007). The resulting instantaneous elastic
100 deformation of the sea floor is eventually smoothed (Kajiura, 1963) to obtain a static sea surface
101 anomaly, that generates waves owing to gravity. The tsunami propagation is then numerically
102 computed in the nonlinear shallow water approximation (Stoker J. J., 1992) until the coastal
103 inundation, fully neglecting dispersive wave effects.
104
105 However, the rupture process has a finite duration and the zones affected by elastic dislocation
106 change as the seismic rupture expands. The spatial and temporal scales of the seismic rupture
107 process, controlled by roughness, size and speed, have a wide range of variability making the
108 above-mentioned approximations valid depending on specific applications (see Abrahams et al.,
109 2023 and references therein). At the first order, we can characterize the scales through the duration
110 and extent of the initial sea level perturbation which, in turn, can be related to the average rigidity
111 and the stress drop of the seismic source (Bilek & Lay, 1999; Geist & Bilek, 2001). On the other

112 hand, the generation process cannot always be accurately modelled as an instantaneous
113 deformation smoothed with a Kajiura filter as input to a shallow water model to propagate the
114 initial static displacement. For slow ruptures, or short-wavelength sea bottom displacements, a
115 more accurate modelling of the time-dependent coupling between the sea bottom and the water
116 layer, and of the subsequent tsunami evolution may be necessary (see, as well, the discussion in
117 Abrahams et al., 2023 and references therein). Beyond that, several numerical comparisons against
118 experimental data (Ma et al., 2012; Macías et al., 2021a, 2021b) demonstrated that accounting for
119 dispersive effects is essential for faithfully simulating waves in the vicinity of the continental shelf,
120 as well as to model run-up, shoaling, and wet-dry areas. Although in a different tectonic setting
121 (outer-rise normal faulting) the dispersive effects might amplify tsunami waves (Baba et al., 2021).
122 To enhance the model's non-linear dispersive properties, it is crucial also to include information
123 on the vertical structure of the flow. In Macías et al. (2021a, 2021b), waves generated after rigid
124 or granular landslides were found to be high frequency and dispersive, with the generated flows
125 exhibiting a complex vertical structure.
126
127 Here, we aim to address if and for which cases a modelling of time-dependent rupture complexity
128 and non-hydrostatic regime accounting for a more physically realistic modelling of seismic source
129 and tsunami processes, respectively, are necessary to guarantee the accuracy of the results for the
130 forecasting of tsunamis generated by large earthquakes in subduction zones. At the same time, we
131 approach this problem keeping in mind the compromise between accuracy and computational
132 demand for practical applications. Thus, a complementary goal is to identify, depending on the
133 cases, which is the minimum computational effort needed to preserve an acceptable accuracy in
134 the results.
135 In this work we start with the 1D time-dependent sea-level displacement (along the x -direction of
136 the sketch in Figure 1a) generated by a 1D numerical model of the seismic rupture (Murphy et al.,
137 2016, 2018; Scala et al., 2017, 2019). This displacement is the input for the 1D tsunami generation
138 and evolution with a non-hydrostatic 3-layer tsunami code (Escalante et al., 2019, 2023). The
139 bathymetry and topography adopted in this study are simplified 1-D versions of transects
140 perpendicular to the coast of Tohoku in Japan. This setup is used as the 'ground-truth' to
141 benchmark more simplified approaches using either instantaneous seafloor displacement, or a one-
142 layer shallow water scheme, or a combination of the two. Although we are aware of the limitations
143 of the 1D approach, it allows us to perform a large number of simulations spanning a broad range
144 of rupture velocities and extensions on different bathymetric profiles and coastal slopes, and with
145 enough spatial resolution to perform inundation modelling. The metrics used to validate the
146 different approaches/approximations are the sea-surface evolution, the offshore maximum wave
147 amplitude at different depths, seaward and landward from the trench, the flow depth and the
148 maximum runup inland.
149 The paper is organized as follows: the coupled modeling of earthquake and tsunami and the
150 numerical setup are presented in sections 2 and 3, respectively. In section 4 the results are
151 described, while discussions about results and final remarks can be found in sections 5 and 6,
152 respectively.

153 2 Methods: Coupling modelling of earthquake and tsunami

154   2.1 Earthquake rupture dynamics modelling

155 To model 1D earthquake rupture dynamics in a 2D elastic domain, we used the same approach
156 proposed in Scala et al. (2017, 2019). We solve the general elastodynamic problem:
157

$$\begin{cases} \rho(x)\ddot{u}(x,t) = \vec{\nabla} \cdot \sigma(x,t) \\ \sigma(x,t) = c(x) : \vec{\nabla}u(x,t) \end{cases} \tag{1}$$

158 In equation (1), x is the position, t the time, $\rho(x)$ is the bulk density, $\sigma(x,t)$ and $c(x)$ the stress
159 and the elastic coefficient tensors respectively, while $u(x,t)$ represents the particle displacement.
160 The traction $T = \sigma \cdot n$ is imposed to be zero on the seafloor interface, neglecting the acoustic
161 coupling between the seafloor and the water itself.
162
163 The fault is modelled through a domain decomposition around a 1D interface where the continuity
164 of the traction T is imposed. The fault slip and slip rate are defined as $\delta u(\tilde{x},t) = u_2(x_2,t) -$
165 $u_1(x_1,t)$ and $\delta v(\tilde{x},t) = v_2(x_2,t) - v_1(x_1,t)$ respectively, with $\tilde{x}$ representing a generic point on
166 the interface while the subscripts 1 and 2 mark the quantities computed on the two sides of the
167 fault. The contact between the two sides of the fault is modelled through the Signorini's condition:
168 the normal traction is either negative and hence the two lips are in contact and prone to frictionally
169 slide or equal to zero, making each side of the interface a free surface and generating an opening
170 (see also eq. (2) in Scala et al., 2019). When the two sides of the fault interface are in contact, the
171 frictional sliding is governed by the following Coulomb condition:
172

$$\begin{cases} [T^t(\tilde{x},t) - C(\tilde{x}) + fT^n(\tilde{x},t)] \cdot |\delta v^t(\tilde{x},t)| = 0 \\ \qquad [T^t(\tilde{x},t) - C(\tilde{x}) + fT^n(\tilde{x},t)] \leq 0 \end{cases} \tag{2}$$

173 In equation (2), the superscripts t and n represent the tangential and normal directions with respect
174 to the interface, C is a level of remote cohesion on the fault that is assumed to decrease to zero
175 approaching the free surface. The friction f is here assumed to linearly decrease with slip from a
176 static level f_s to a dynamic one f_d over a finite length of slip D_c (Slip weakening; Ida, 1972).
177 Elastodynamic equations with a sliding interface are numerically solved through a 2D Spectral
178 Element Method (SEM, Komatitsch & Vilotte, 1998) where quadrangular elements are discretized
179 using $9x9$ Gauss-Lobatto-Legendre nodes, ensuring at least 5 points for the minimum propagating
180 wavelength and at least 4 points to model the fault cohesive zone (Scala et al., 2017).The free
181 surface is naturally modelled in SEM while the other boundaries mimic an infinite half-space
182 through the implementation of PMLs (Festa & Vilotte, 2005).
183 A Newmark second order forward time scheme is implemented with an average Courant number
184 of about 0.04. Such a small value allows to model the shallowest part of the domain honouring the
185 shape of the domain between the fault and the free surface, and ensuring the stability also in the
186 stretched elements within this wedge.
187 The fault is modelled as a planar interface embedded in a homogeneous medium and forming a
188 dip angle $\delta = 20°$ with the horizontal direction similarly to what proposed by Scala et al., (2019).
189 The free surface, in turn, is inclined of an angle $\alpha = 3.5°$ with respect to the horizontal direction,
190 this value being an average of the bathymetry slopes for the different profiles in the vicinity of the
191 trench (Figure 1). Since we aim to model a simplified Tohoku-like environment in terms of fault

192 geometry and topo-bathymetric distributions (see Section 2.4 for more details), the dip angle
193 represents an average value between the almost horizontal trench and the steeper slope of the deep
194 crust-mantle interface as shown in other works (Kozdon & Dunham, 2013; Murphy et al., 2018)
195 implementing 1D extrapolations of Slab 2.0 modelling (Hayes et al., 2018).
196 The remote stress field is oriented to mimic the combination of a vertical lithostatic and a
197 horizontal tectonic loading. Their components are compatible with a reverse frictional sliding
198 mechanism as expected for interface subduction events. On the fault interface the initial normal
199 traction $T_0^n(\tilde{x}, t)$ linearly increases to mimic the increase of lithostatic loading (Huang et al., 2012;
200 Murphy et al., 2016, 2018). The static and the dynamic friction coefficients f_s and f_d are imposed
201 to be equal to 0.25 and 0.05 respectively to prevent the opening at the free surface (Scala et al.,
202 2019). The strength excess $s = (f_s T_0^n - T_0^t)/(T_0^t - f_d T_0^n)$ is set to 2 on the entire interface to
203 avoid the acceleration of rupture toward supershear regimes (Burridge, 1973), since it was never
204 observed during the largest reverse subduction tsunamigenic earthquakes. Therefore, the shear
205 strength $f_s T_0^n$ the dynamic level $f_d T_0^n$, the initial shear stress T_0^t and the local stress drop $T_0^t -$
206 $f_d T_0^n$ increase with depth accordingly to T_0^n. A cohesion C vanishing toward the fault-free surface
207 intersection is imposed with a value of about 10% of the maximum stress
208 All the input/output physical quantities are normalised to infer general results from the simulations.
209 The slip on the fault δu and the ensuing displacement on the surface d are normalised by means
210 of the critical slip weakening distance leading to the dimensionless parameters $\widetilde{\delta u} = \delta u/D_c$ and
211 $\tilde{d} = d/D_c$. All the tractions T are normalised through the maximum stress drop on the fault $\Delta\sigma_0$
212 as $\tilde{T} = T/\Delta\sigma_0$. The distances z, including the fault extension W and the ensuing tsunami source
213 size λ (See Figure 1), and the time t are normalised as $\tilde{z} = \frac{\Delta\sigma_0}{\mu D_c} z$ and $\tilde{t} = \frac{V_s \Delta\sigma_0}{\mu D_c} t = \frac{\Delta\sigma_0}{V_s \rho D_c} t$
214 respectively. In these two latter normalisation factors, μ and ρ are the medium rigidity and density
215 respectively with $V_s = \sqrt{\mu/\rho}$ the S-wave propagation velocity. This setup allows us to define an
216 ensemble of different tsunami sources featuring a broad range of source extensions and durations
217 running a single dimensionless earthquake simulation and selecting parameters like $D_c, \Delta\sigma_0, \mu$ and
218 ρ in realistic ranges constrained by observations (see details in Section 3).
219 To trigger the spontaneous crack, we defined an asperity featuring an initial shear stress larger than
220 the shear strength and having a size L_c large enough to allow the rupture to move away from the
221 nucleation zone (Uenishi & Rice, 2003) .The nucleation asperity is placed at an intermediate depth
222 with respect to the whole domain. Previous numerical experiments have shown that this is the
223 preferential nucleation depth to generate events rupturing the whole domain and hence to describe
224 the behaviour of a megathrust earthquake (Murphy et al., 2018).

225   2.2 Tsunami modelling

226
227 We used a multilayer shallow-water non-hydrostatic model. The multilayer approach was
228 introduced by Audusse et al. (2011) and Fernández-Nieto et al. (2014) to capture vertical effects
229 in shallow flows. The equations are depth-averaged at every layer, leading to a layer-wise constant
230 approximation. Such a technique was already efficiently applied to landslide-generated tsunamis
231 (Macías et al., 2021a) and for dry granular flows (Escalante et al., 2023a). Concerning dispersion,
232 following the pioneering work of Casulli (1999), non-hydrostatic effects are incorporated into the
233 shallow water framework by splitting the total pressure into hydrostatic and non-hydrostatic
234 components, providing a given profile for the non-hydrostatic component and the vertical velocity,

235 together with the incompressibility condition. This approach has been recently further developed
236 improving the dispersive layer-averaged approximations (Fernández-Nieto et al., 2018; Escalante
237 et al., 2023b), and efficiently GPU-implemented using finite volume and finite difference schemes
238 (Escalante et al., 2018). A vertical discretization of the fluid into several layers only approximates
239 the physics of the fluid. The number of layers can be increased to bring the system close to three-
240 dimensional solvers, becoming able of adequately describing the vertical structure of the flow.
241 That leads to notable improvements in the dispersion properties of the model. The multilayer
242 model used in this study is the following (see, Fernández-Nieto et al., 2018):
243

$$\partial_t h + \partial_x(h\bar{u}) = 0,$$
$$\partial_t(h_\alpha u_\alpha) + \partial_x(h_\alpha u_\alpha^2) + g h_\alpha \partial_x \eta + u_{\alpha+1/2}\Gamma_{\alpha+1/2} - u_{\alpha-1/2}\Gamma_{\alpha-1/2}$$
$$= -\frac{1}{2}h_\alpha \partial_x(p_{\alpha+1/2} + p_{\alpha-1/2}) + (p_{\alpha+1/2} - p_{\alpha-1/2})\partial_x z_\alpha + K_{\alpha-1/2} - K_{\alpha+1/2} - \tau_\alpha^u, \quad (3)$$
$$\partial_x(h_\alpha w_\alpha) + \partial_x(h_\alpha w_\alpha u_\alpha) + w_{\alpha+1/2}\Gamma_{\alpha+1/2} - w_{\alpha-1/2}\Gamma_{\alpha-1/2} = -h_\alpha(p_{\alpha+1/2} - p_{\alpha-1/2}) - \tau_\alpha^w.$$

244
245 In the system (3), $h(x,t)$ represents the total water height at each point $x \in \Omega \subset R$, and time $t \geq$
246 0, where Ω is the considered (horizontal) domain. The water height is decomposed along the
247 vertical axis into a prescribed number of layers $L \geq 1$ (see Figure S1 in Supporting Information).
248 For any layer α, its thickness will be assumed to be $h_\alpha = l_\alpha h$, for some values $l_\alpha \in (0,1)$ such
249 that $\sum_{\alpha=1}^{L} l_\alpha = 1$. Usually, $l_\alpha = 1/L$ is selected. The upper and lower interfaces of the layer α are
250 represented by $z_{\alpha+1/2}$ and $z_{\alpha-1/2}$, respectively, that is, $z_{\alpha+1/2} = z_b + \sum_{\beta=1}^{\alpha} l_\beta h$. The uppermost
251 interface corresponds to the sea surface, denoted by $\eta(x,t) = h(x,t) + z_b(x,t)$; the lowermost
252 one corresponds to the seafloor basin represented by $z_b(x,t)$, which is supposed to be perturbed
253 by the earthquake. Finally, $z_\alpha = \frac{1}{2}(z_{\alpha-1/2} + z_{\alpha+1/2})$ denotes the level of the middle point of the
254 layer. The depth-averaged velocities in the horizontal and vertical directions are written as
255 $u_\alpha(x,t)$, and $w_\alpha(x,t)$, respectively. Finally, $p_{\alpha+1/2}$ denotes the non-hydrostatic pressure at the
256 interface $z_{\alpha+1/2}$, and is assumed to be 0 at the free surface. The mean of the depth-averaged
257 horizontal velocities is indicated by $\bar{u} = \sum_{\alpha=1}^{L} l_\alpha u_\alpha$.
258 Moreover, for any field $f \in \{u, w\}$, we denote $f_{\alpha+1/2} = \frac{1}{2}(f_{\alpha+1} + f_\alpha)$. As usual $g = 9.81 \ m/s^2$
259 is the gravity acceleration and $\Gamma_{\alpha+1/2}$ parametrizes the mass transfer across interfaces:
260

$$\Gamma_{\alpha+1/2} = \sum_{\beta=\alpha+1}^{L} \partial_x\left(h_\beta(u_\beta - \bar{u})\right), \quad (4)$$

261 where we assume no mass transfer through the seafloor or the free surface ($\Gamma_{1/2} = \Gamma_{L+1/2} = 0$).
262 Each layer is supplemented with the following divergence-free constraint $\mathcal{I}_\alpha = 0$, $\alpha \in \{1,2,\dots,L\}$,
263 where
264

$$\mathcal{I}_\alpha = h\alpha\partial_x u_\alpha + 2\bar{w}_{\alpha+\frac{1}{2}} - 2w_\alpha,$$
$$\bar{w}_{\alpha+\frac{1}{2}} = \partial_t z_b + u_\alpha \partial_x z_{\alpha+1/2} - \sum_{\beta=1}^{\alpha} \partial_x(h_\beta u_\beta), \quad (5)$$

265

266 and the term $\partial_t z_b$ accounts for the movement of the bottom interface.

267 Note that the system is endorsed with extra dissipation accounting for friction with the bottom
268 (τ_α^u), for viscous terms that model the shear stresses between the layers ($K_{\alpha\pm1/2}$), and for the
269 breaking of the waves near the coast (τ_α^w). Here, we used the following dissipation models
270 proposed by Macías et al. (2021a)
271 For the friction effects between the water and the seafloor, we used a standard Gauckler-Manning
272 friction formula applied to the lowest layer

$$\tau_\alpha^u = \begin{cases} gLn^2|u_1|\dfrac{hu_1}{h^{4/3}}, & \alpha = 0 \\ 0, & \alpha \in \{2, \dots, L\} \end{cases} \tag{6}$$

273

274 We followed a simplified version of the model presented in Bonaventura et al. (2018) for the shear
275 stress between the layers

$$K_{\alpha+1/2} = -\nu\frac{u_{\alpha+1} - u_\alpha}{(h_{\alpha+1} + h_\alpha)/2} \tag{7}$$

276 where ν is a constant kinematic viscosity, and $K_{1/2} = K_{L+1/2} = 0$.

277 For the breaking dissipation model, we considered here an extension of the simple, efficient, and
278 robust model considered in Escalante et al. (2019) for a two-layer model:

$$\tau_\alpha^w = C\, w_\alpha\, |\partial_x(hu_\alpha)|, \quad \alpha \in \{1, \dots, L\} \tag{8}$$

279 The coefficient $C(x, t)$ defines breaking criteria to switch on/off the dissipation of the energy due
280 to the presence of a breaking wave (e.g., Roeber et al., 2010). Here, we used

$$C = \begin{cases} 35\left(\dfrac{|\bar{u}|}{0.4\sqrt{gh}} - 1\right) & \text{if } |\bar{u}| > \sqrt{gh}, \\ 0 & \text{if } |\bar{u}| \leq \sqrt{gh}. \end{cases} \tag{9}$$

281

282 The system in equations (3)-(5) satisfies an energy balance equation (Fernández-Nieto et al.,
283 2018). The used modelling includes the non-hydrostatic ocean response and accurately captures
284 dispersion and related effects during tsunami propagation and generation (Ma et al., 2012; Macías
285 et al., 2021a, 2021b). Using a standard, Stokes-type, Fourier analysis for the linearized version of
286 equations (3)-(5) around the water at rest steady-state, the phase, group velocities, and linear
287 shoaling gradient are determined and compared with the Airy or Stokes linear theory for different
288 numbers of layers (see Figure S2 in the Supporting Information, where relative errors are shown
289 for the phase and group velocities, as well as for the shoaling gradient). One can prove uniform
290 convergence for the analytical values when the number of layers increases (Fernández-Nieto et al.
291 2018).

292 A detailed description of the numerical discretization and implementation of this model, along
293 with the comparison of results with standard benchmark problems, were presented in Text S1 and
294 Text S2 of Supporting Information.

295 **3 Numerical setup and the simulated dataset**

296 The time-dependent vertical displacements caused by the dynamic rupture simulations are used as
297 generation mechanism for the tsunami simulations. The displacement of the bathymetry and of the
298 topography are both considered. The intersection between the fault and the free surface (the
299 seafloor) coincides with the deepest point of the bathymetry and corresponds to the trench (see
300 sketch in Figure 1a). The zero height of the bathymetry represents the initial sea level and positive
301 values represent the topographic elevation of the coast. The sea surface elevation for all the grid
302 points, both offshore and inland, is collected each 30 seconds. All the tsunami simulations last 2
303 hours.

305 One example of the dimensionless sea floor deformation at various times during one simulation is
306 shown in Figure1(b). The distance from the trench is meant along the horizontal direction. It is
307 worth to notice that the final static deformation (yellow curve in Figure 1b) might feature a lower
308 maximum amplitude with respect to the transient deformation occurring previously (green curves
309 in Figure 1b). This effect is due to the surface deformation induced by the trapped waves within
310 the wedge as already shown by Oglesby et al. (2000) and Scala et al. (2019). A secondary vanishing
311 deformation with a maximum amplitude of about 25% of the final static displacement, still due to
312 the propagating seismic waves, triggers a tsunami wave propagating rightward from the trench
313 ahead of the main wave.

315 Starting from a single dimensionless seismic rupture simulation, a broad range of different tsunami
316 sources can be modelled. Exploiting the normalization presented in Section 2.1, we can vary the
317 rigidity μ and the density ρ of the medium, the stress drop $\Delta\sigma$ of the earthquake and the
318 characteristic slip weakening distance D_c, to obtain different durations, maximum amplitudes, and
319 lateral extensions. The event size is then directly connected to the characteristic tsunami source
320 wavelength.

322 The rigidity and the density are selected to cover a broad range of elastic properties which typically
323 characterize the slab interfaces at the characteristic seismogenic depths, integrating values from
324 reports released by Earthquake Research Promotion of Japanese Government (available at
325 https://jishin.go.jp/main/chousa/17apr_chikakozo/model_concept-e.pdf, with densities
326 extrapolated through Ludwig et al., 1970) and from several tomographic models for the Japanese
327 slab (e.g. Takahashi et al., 2004; Yamada & Iwata, 2005; Miyake et al., 2008). The sampled
328 rigidity, density values, the shear wave velocity $V_s = \sqrt{\mu/\rho}$ and the corresponding subduction
329 layers, are reported in Table S1 of Supporting Information.

331 The stress drop values are sampled in a range between 0.2 and 30 MPa according to general
332 observations about crustal, downdip interplate and tsunami earthquakes (Kanamori & Brodsky,
333 2004; Venkataraman & Kanamori, 2004; Bilek et al., 2016; Abercrombie et al., 2017; Folesky et
334 al., 2021). Within this range, we selected 15 values such that their logarithms are equally spaced.
335 A single characteristic slip weakening distance is selected ($D_c = 2\ m$) leading to a maximum slip
336 $\delta u \sim 15\ m$ for the rupture dynamic simulations. This value is consistent with the one extrapolated
337 for a $M_w = 9.0$ event according to the scaling law proposed by Skarlatoudis et al. (2016).

339 Combining all the sampled parameters, 345 different tsunami initial conditions could be set.
340 However, most of them lead to either unrealistic or out of range of interest seismic source size.

341   The smallest rigidity values cannot be associated indeed with large stress drops and vice versa, to
342   avoid modelling too small and too large earthquakes, respectively. Imposing a range of fault widths
343   compatible with the expected value ($\pm 1\sigma$) of the scaling relations proposed by Strasser et al.
344   (2010) for a magnitude interval $8.0 \leq M_w \leq 9.0$, we selected 81 out of the 345 combinations of
345   parameters (See figure S9a and Table S2 in Supporting Information).
346   Each parameter combination leads to a characteristic source duration $\tau = \tau' \mu D_c / (\Delta\sigma V_s)$ and to
347   an along-dip source size $W = W' \mu D_c / \Delta\sigma$, with $\tau' = 17.1$ and $W' = 8.3$ representing the
348   dimensionless duration and width computed through the dynamic rupture simulation. From τ and
349   W values a proxy of rupture velocity V_r can be estimated (Figure S9b in Supporting Information).
350   The rupture duration ranges between 25 s and 570 *s,* while $0.2 km/s \leq V_r \leq 2.3 km/s$, these
351   values fitting the common observations for recent tsunamigenic earthquakes (Yoshimoto &
352   Yamanaka, 2014; Ye et al., 2016). In the next section, all the results will be presented as a function
353   of τ, W and the ratio $\tau/W \propto 1/V_s$ that represents a size-normalized rupture duration and hence a
354   measure of the characteristic rupture slowness. Some of the results will be presented as a function
355   of $\lambda = W \cdot cos(dip) = W \cdot cos(20°)$ as indicated in Figure 1(a). This last quantity is the
356   horizontal maximum extension of the seismic source and within this simple geometrical model
357   represents a proxy of the characteristic wavelength of the source. The longest durations owe to
358   small values of rigidity and stress drops, in turn deriving from shallow-depths rheological
359   conditions, while the fastest sources are associated with large values of rigidity and stress drop, a
360   more realistic condition for deeper events (Bilek & Lay, 1999; Geist & Bilek, 2001; Ebeling &
361   Okal, 2012; Okal et al., 2016).Within this framework, the choice of a logarithmic scale for the
362   stress drop along with the large number of models featuring small rigidity values (Table S2 in
363   Supporting Information) allows us to more finely sample sources characterized by longer duration
364   which are expected to mostly detach from the standard instantaneous source modelling.

365

366   We considered the time-dependent 3-layer non-hydrostatic model (hereinafter TD-NH) as the
367   reference and we compared against it the simplified models (instantaneous source and shallow
368   water, hereinafter IS and SW respectively). For the aim we simulated each initial condition 4 times
369   (TD-NH, IS-NH, TD-SW and IS-SW). The IS were simulated imposing an instantaneous seafloor
370   deformation equals to the final static displacement (as the yellow curve in Figure 1b). SW is
371   simulated through a single layer hydrostatic approximation, and we used a Manning friction
372   coefficient equal to 0.025. A constant Courant number equal to 0.9 is imposed. All these choices
373   are justified by the performed tests, described in sections TextS1 and TextS2 in Supporting
374   Information

375

376   The comparison is performed through three metrics: the wave amplitude η (sea surface elevation
377   with respect to the still water level) and its maximum η_{max} at offshore gauges, the flow-depth *D*
378   and its maximum D_{max} at onshore gauges (the water amplitude onto the topographic elevation)
379   and the maximum run-up R_{max} that is the maximum topographic elevation reached by the tsunami
380   during the inundation. For any metrics *K* we defined the discrepancy ΔK as the relative error due
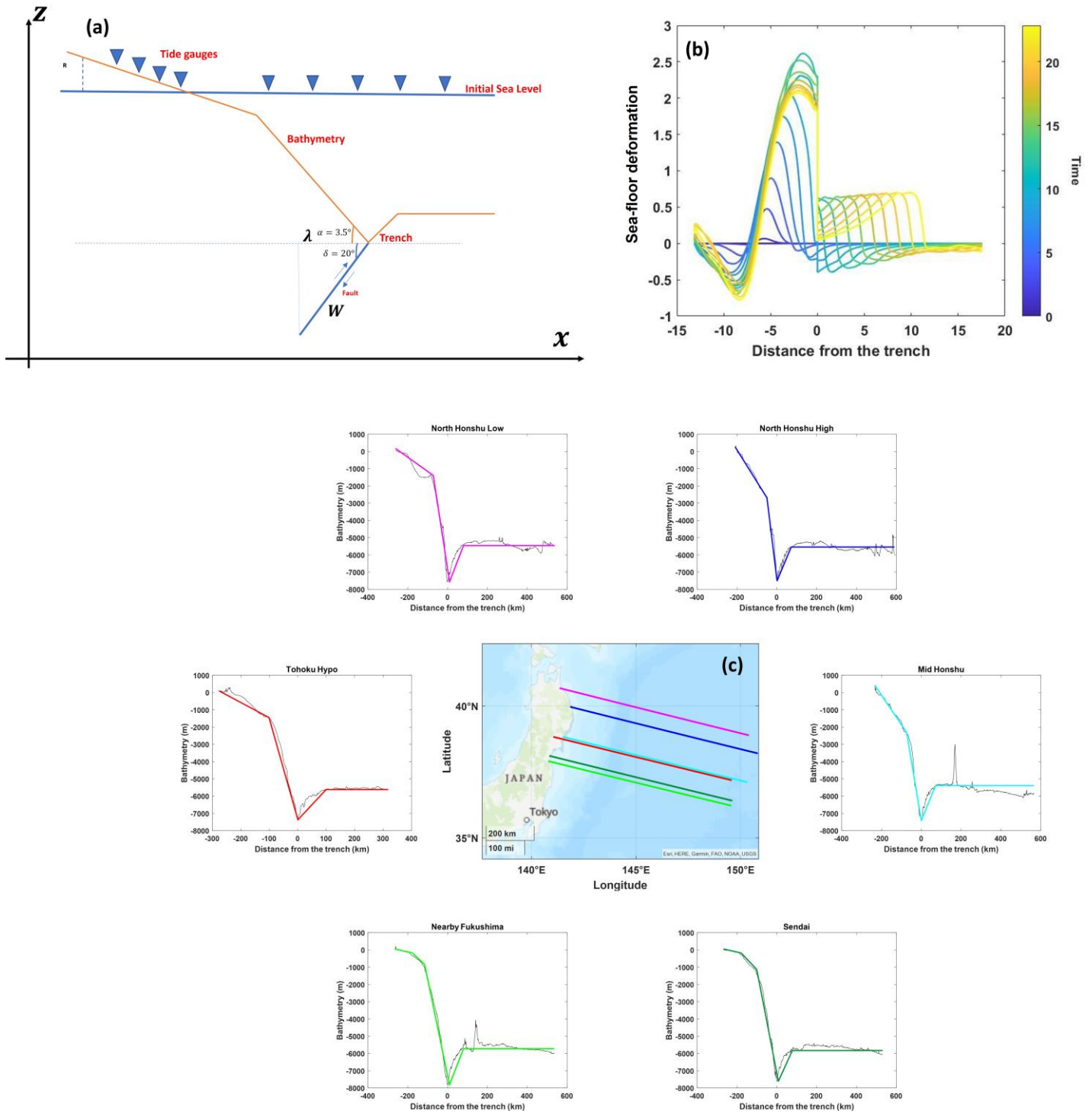381   to the use of a simplified model:

382

$$\Delta K = \frac{K_{ref} - K_{simpl}}{K_{simpl}} \qquad (10)$$

383
384   ΔK might assume negative values indicating that a simplified model produces an overestimation
385   with respect to the reference one.
386
387   To investigate how much the results depend on the coupling between the tsunami and the oceanic
388   and coastal morphology, the initial deformations are projected onto 6 different 1D topo-
389   bathymetric profiles (colored lines on the map of Figure 1c). Each profile (blue lines in the insets
390   around the map in Figure 1c) is extracted from the 30 arc-sec model SRTM30+
391   (https://topex.ucsd.edu/WWW_html/srtm30_plus.html) and then simplified to obtain piece-wise
392   linear depth variations (colored profiles in the insets of Figure 1c) characterized by a planar scarp
393   combined with either a planar or a segmented shelf towards and beyond the coast. This
394   simplification allows to limit the effect of short size discontinuities and to provide general
395   considerations about the effects depending on the large-scale geometrical features. The scarp
396   slopes are quite similar to each other and are characterized by an average angle of 3.5° among the
397   6 profiles. Conversely, in the vicinity of the coast, the slopes are gentler in the southern part of the
398   Tohoku region (Sendai and Fukushima areas), and steeper in the northern part (Iwate prefecture)
399   with an intermediate behavior along the profile containing the nucleation area of the Tohoku
400   earthquake. The mainland is modelled as a single slope. Most of the results presented in the next
401   section will be obtained for the Tohoku nucleation area (red profile and bathymetry in Figure 1c)
402   while a comparison between the different bathymetries is shown in section 4.3.
403
404   To ensure enough spatial resolution we performed a preliminary convergence test, running
405   equivalent simulations on 6 grids characterized by different space sampling $\Delta x =$
406     $[500m; \; 250m; \; 125m; \; 62,5m; \; 31,25m; \; 15,625m]$. We tested the discrepancy of each grid with
407   respect to the finer one (assumed as a reference) computing the $\Delta_{\eta_{max}}$ offshore and the $\Delta_{D_{max}}$ on
408   the coast similarly to eq. (**10**) but considering the module of the difference as numerator and the
409   value on the finest grid as denominator. With this definition the Δ values represent the relative
410   errors due to the use of a rougher grid. This analysis has been carried out extracting η_{max} and
411   D_{max} at fixed gauge positions (regardless of the time at which these maxima are recorded) for
412   two end-member initial conditions that is the largest size event (ID 1 in Table S2, $W = 275.3 \; km$)
413   and the smallest size one (ID 81 in Table S2 $W = 57.06 \; km$) respectively. We retrieved $\Delta_{\eta_{max}} <$
414   5% everywhere and for both tests, already with rather rough grids (up to $\Delta x = 125 \; m$ offshore
415   and $\Delta x = 62.5 \; m$ in the vicinity of the coast, Figures S10c and S10d in Supporting Information).
416   However, $\Delta_{D_{max}}$ is below the threshold only for $\Delta x = 31,25 \; m$ in the vicinity of the maximum
417   run-up position at least for the smallest size simulations (see Figure S10a in Supporting
418   Information). Since one of our aims is to model with enough accuracy the inundation features,
419   including the maximum run-up, we finally used $\Delta x = 31,25 \; m$ for the whole simulation dataset.

420

Figure 1: Schematic description of the simulation setup. (a) Sketch of the geometrical setup. The angle between the bathymetry (orange line) and the horizontal dashed line is exaggerated for sake of clarity. The blue triangles represent the gauges where the wave amplitude is computed both inland and offshore. W and λ represent the width on the fault and the horizontal extension of the surface deformation respectively. (b) Time dependent vertical topo-bathymetric deformation as a function of the distance from the trench. The time increases from blue to yellow curves with a final static deformation featuring a lower maximum with respect to the transient deformation occurring before. All the variables are plotted as dimensionless parameters. (c) Different modelled bathymetries. The modelled bathymetries are extracted from the 1D profiles in the map. Within the insets the bathymetry variation for each profile is plotted as a black line while the simplified geometry used in the simulations is plotted with the same color of correspondent profile in the map.
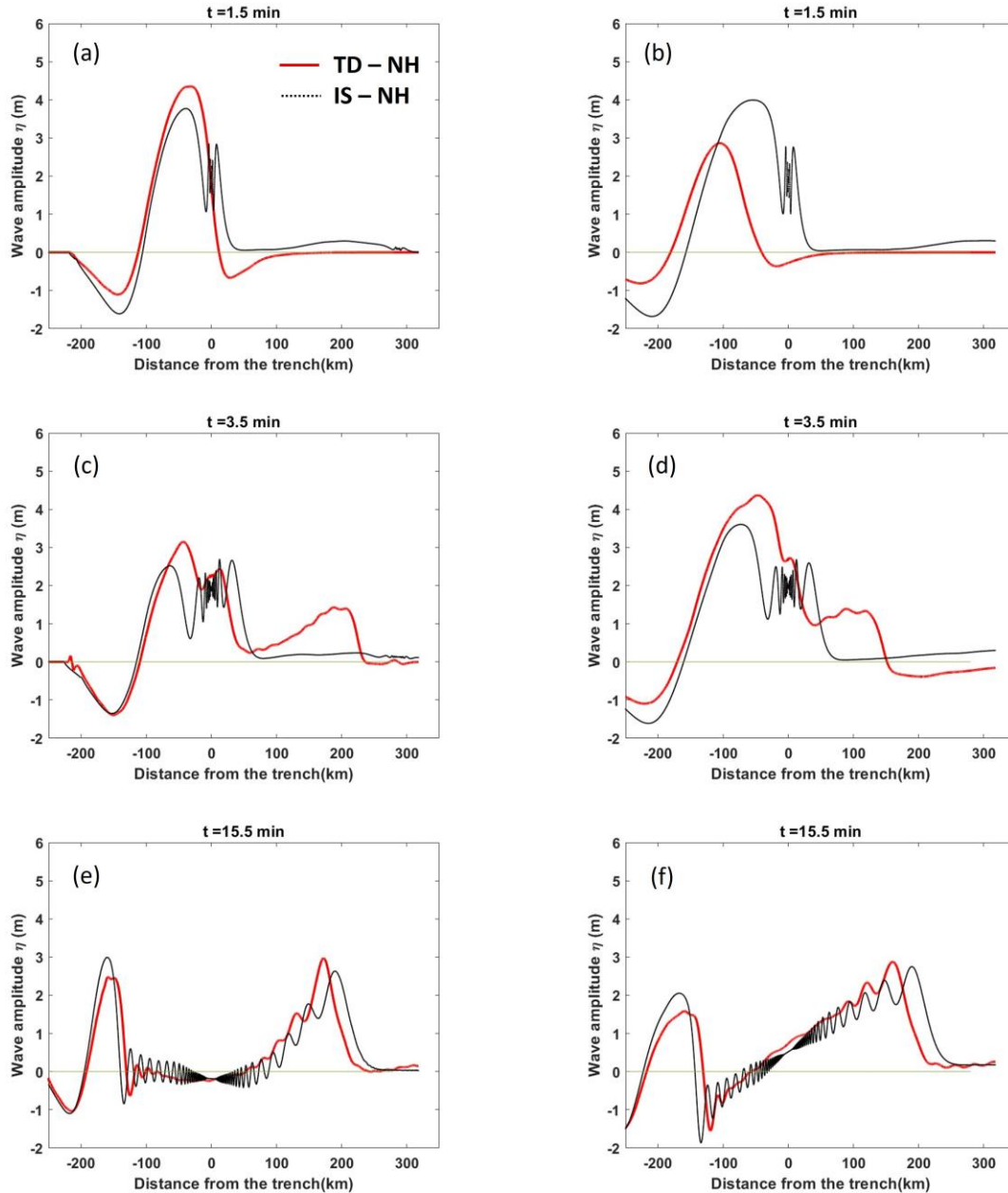
421
422
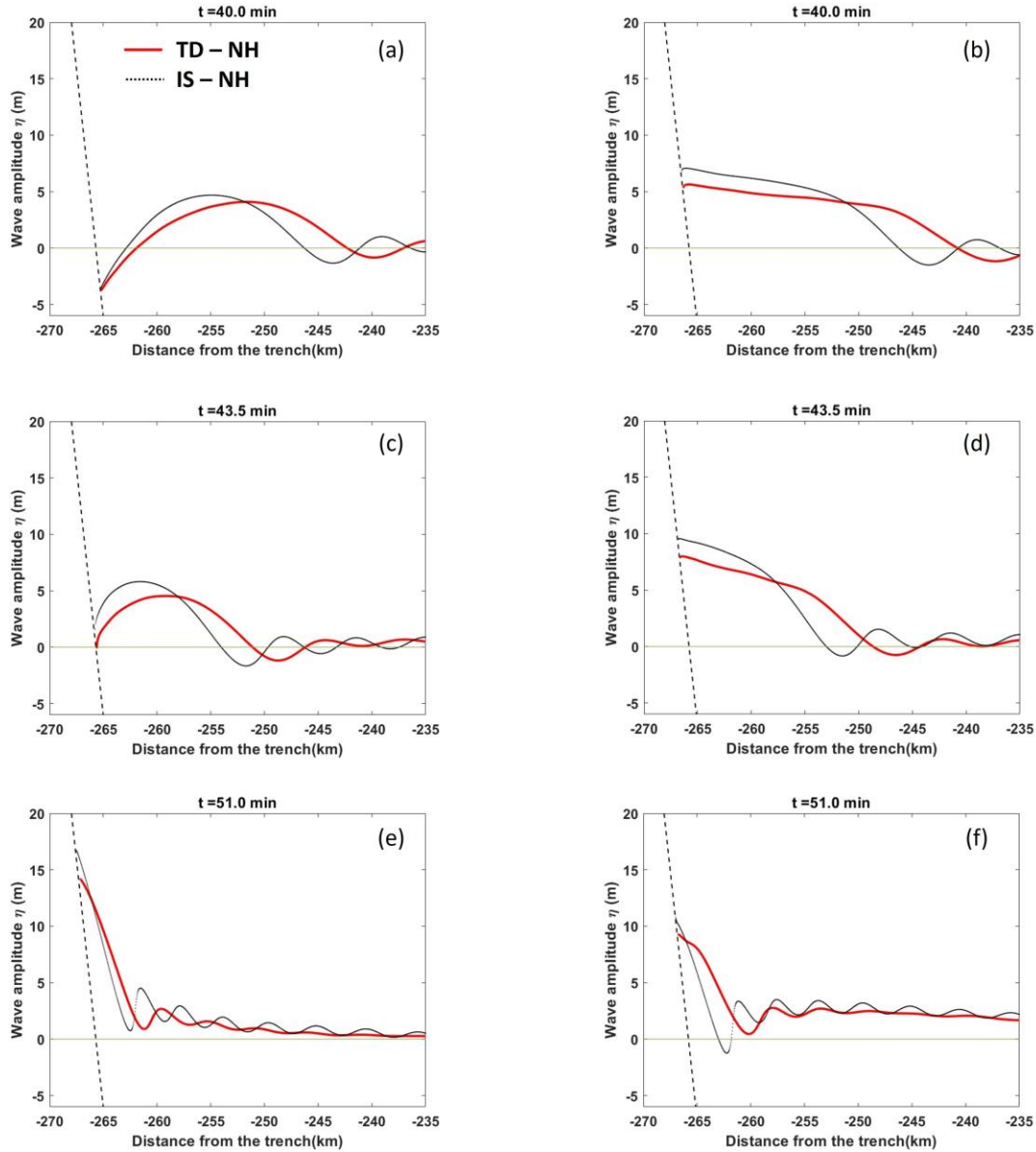
4 Results

4.1 Off-shore and coastal wave amplitude

Time-dependent VS instantaneous source

426 First, we show a qualitative comparison between the water waves generated by the non-hydrostatic
427 time-dependent (TD-NH) and instantaneous sources (IS-NH). Figure 2 shows the wave amplitude
428 as a function of the distance from the trench for two different initial conditions (simulations ID 31
429 and 11 are plotted on the left and right columns respectively, see Table S2 in Supporting
430 Information) at different time steps and for both TD-NH and IS-NH. While the two simulations
431 are characterized by the same τ/W value and hence by an equivalent dynamic evolution, the
432 simulations on the right panels (Figures 2b-d-f) feature a large enough W (and τ) to generate
433 coastal subsidence. For both simulations (small and large W), the TD sources feature a larger
434 maximum wave amplitude than the corresponding IS, and the maxima occurs at various times, as
435 an effect of the different duration of the transient. However, this transient is rapidly attenuated
436 during the landward propagation outside of the source region, and, starting from a certain time, the
437 IS systematically features larger η_{max} with respect to the TD simulation (Figures 2e and 2f).
438 Conversely, towards the open sea, rightward from the trench, we retrieve the opposite behavior
439 with the TD source leading to larger yet delayed maximum η as an effect of the directivity (the
440 seaward motion of the upper plate).
441 Regardless of the source temporal features (TD vs IS), the main difference between simulations
442 with small and large W emerges while the waves are approaching the coast. For small W, such
443 that λ is smaller than half distance between trench and the coast, (Figures 2a-c-e), the wave shoals.
444 For larger ruptures (Figures 2b-d-f), the instantaneous sea drawback limits the shoaling and thus
445 the amplification of the wave close to the coast as can be spotted by comparing Figures 2e and 2f.

Figure 2: Wave amplitude as a function of the distance from the trench for TD – NH (red curves) and IS – NH (black dotted lines) at three different time steps and for two simulations: the ID 31 (left panels) and the ID 11 (right panels) in Table S2 in Supporting Information. These simulations represent examples of small and large-size sources, respectively. The whole evolution can be found in the Supporting Information (Movies S1 and S2).
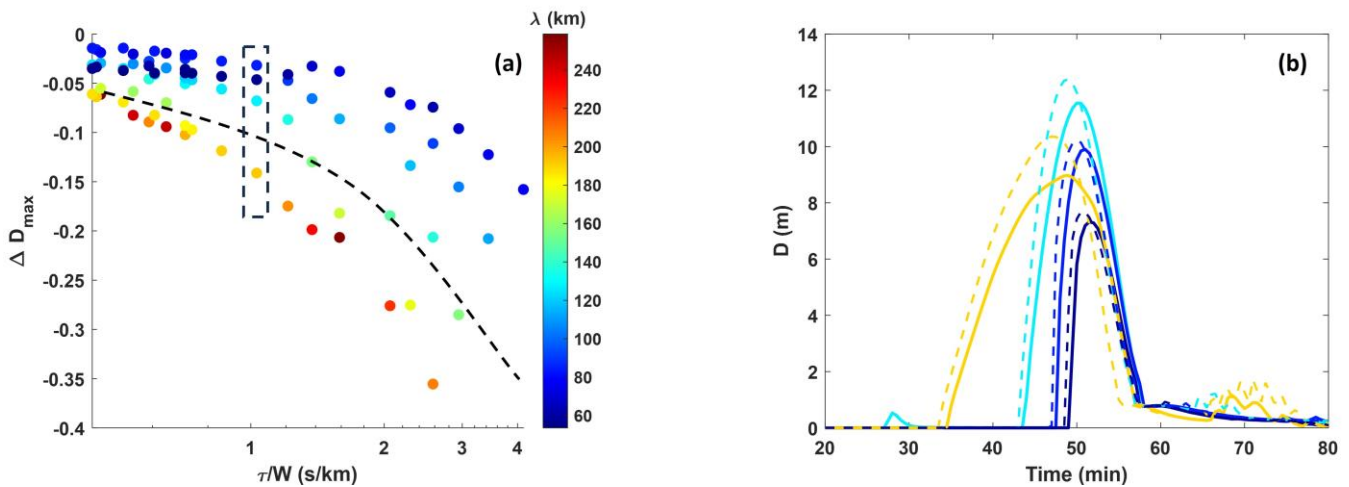
14

Figure 3: Wave amplitudes, zoomed around the coast, as a function of the distance from the trench for TD – NH (red curves) and IS – NH (black dotted lines) at three different time steps and for two simulations: the ID 31 (left panels) and the ID 11 (right panels) in Table S2 of Supporting Information. These simulations represent examples of small and large size sources respectively. The short-dashed line on the left represents the coastline within each panel. The whole evolution can be found in the Supporting Information (Movies S3 and S4).

455

456   This difference is evident also by zooming around the coastline (Figure 3) at a later stage ($t >$
457   40min). From this close-by view, it can also be seen that the inundation begins earlier for rupture
458   with large W (Figure 3b), when for the small W simulation, the tsunami is still in the shoaling
459   phase (Figure 3a). When the large source simulation has almost reached its maximum (Figure 3d),

460 the inundation for the smaller source starts (Figure 3c), reaching in the end a maximum run-up that
461 is about 1.5 times the one for the large W, for both IS and TD sources. This is a direct consequence
462 of the potential energy accumulation during the shoaling process (Figures 3e and 3f). However,
463 independently of the size and duration of the TD source, approximating it with an instantaneous
464 source always results in a larger inundation both in terms of flow-depth D and maximum run-up
465 R_{max}.
466 To systematically quantify the discrepancy between the IS and TD sources, we investigated the
467 variability of $\Delta_{D_{max}}$ at the points on the coast (eq. (**10**)), as a function of τ/W (horizontal axis)
468 and λ (different colors) for all the 81 simulations (see section 3 and Table S2 in Supporting
469 Information). In Figure 4 the results for the first point on the coast are summarized. We observed
470 that the IS source systematically overestimates the flow-depth ($\Delta_{D_{max}}$ values are always negative,
471 Figure 4a). The slower the TD rupture, the larger the discrepancy with the correspondent IS
472 simulation. A second trend depending on the source extension emerges, as for fixed τ/W, larger
473 ruptures lead to larger discrepancies. A comparison between the time histories of the flow-depths
474 at the first point on the coast is shown in Figure 4b, for the simulations inside the dashed rectangle
475 in Figure 4a. The four simulations are characterized by the same source dynamic time scale, that
476 is τ/W, with the larger extension due to a larger stress drop $\Delta\sigma$. The flow-depth amplitude D_{max}
477 increases with λ until a maximum value (cyan curves in Fig. 4b) with an overestimation between
478 3% and 7% due to the instantaneous modelling. For larger λ, D_{max} decreases featuring larger
479 overestimations up to about 14%. This overestimation is particularly significant for the largest λ
480 values, because the inundation directly relates with source time history which becomes dominant
481 given the virtual absence of landward propagation and shoaling. We have verified that comparable
482 results hold when a SW propagation modelling is used, which is important because the most
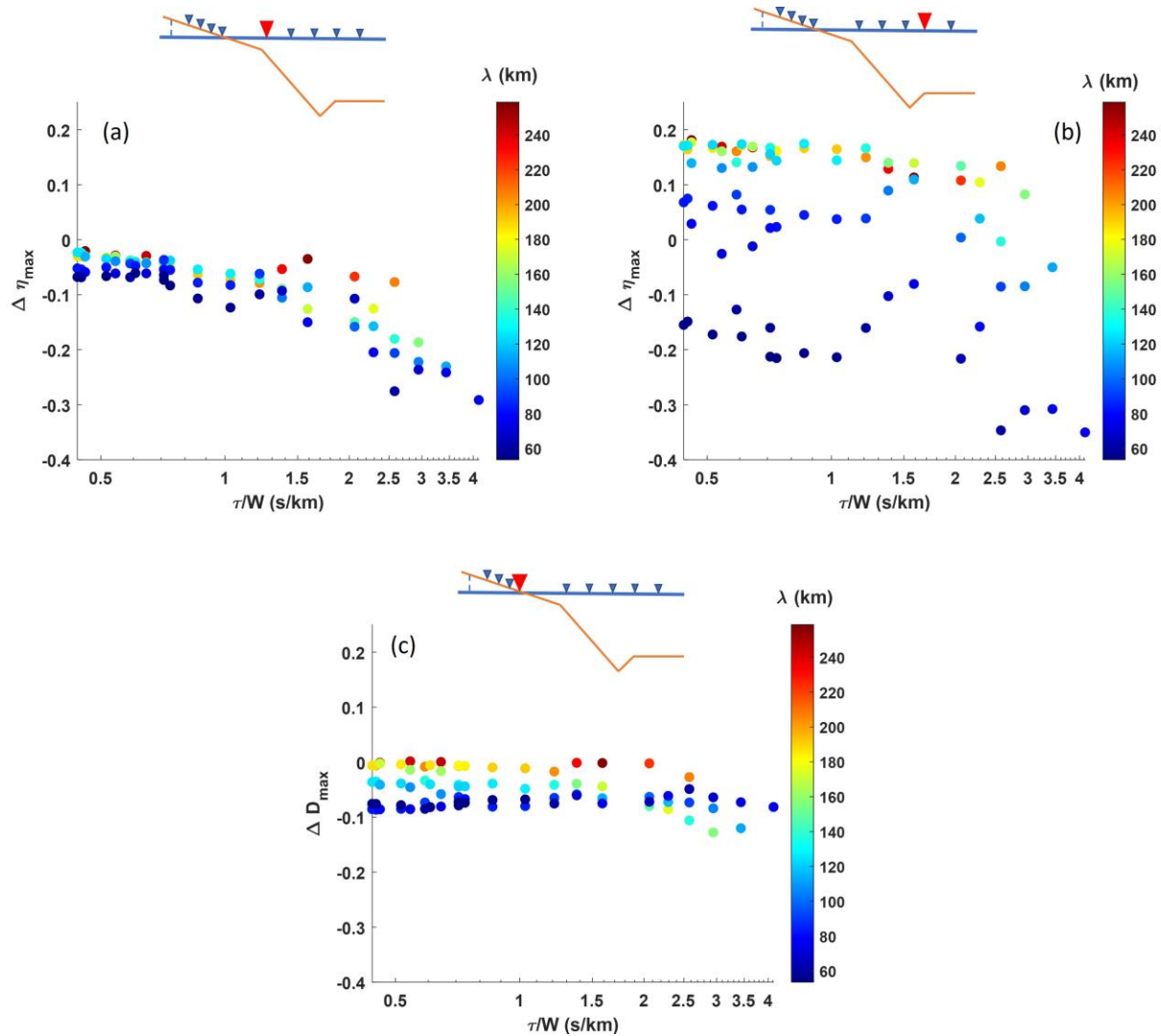483 commonly adopted approximation is the SW-IS approach (Figure S11 of Supporting Information).
484
485

486

487 **Figure 4:** Relative discrepancy between time-dependent (TD-NH) and instantaneous source (IS-
488 NH) results in terms of flow-depth at the first point on the coast (a) ΔD_{max} at the first point on the
489 coast as a function of τ/W with color scale marking the source horizontal extension λ. The black
490 dashed line separates the two highlighted trends for small and large ruptures. (b) Flow-depth as a

491 function of time for the four simulations within the black-dashed rectangle in panel (a) plotted with
492 the same colors. In panel (b) TD and IS sources are represented through solid and dashed lines
493 respectively.

494 **Non-hydrostatic VS Shallow Water propagation**

495 To perform a systematic comparison between the accuracies of NH and SW propagation schemes
496 in modelling a tsunami generated by a TD seismic source, we run a set of SW propagation
497 simulations of tsunamis triggered by the same seismic TD source as used in the NH simulations
498 described in the previous section.
499

500

Figure 5: Relative discrepancy between Non-Hydrostatic (NH) and Shallow Water (SW) results when TD sources are used for both propagation regime. (a) $\Delta\eta_{max}$ at a gauge placed along the coastward propagation as a function of τ/W with color scale marking the source horizontal extension λ. (b) $\Delta\eta_{max}$ at a gauge placed rightward beyond the trench as a function of τ/W with color scale marking the source horizontal extension λ. (c) ΔD_{max} at the first point on coast as a function of τ/W with color scale marking the source horizontal extension λ. For sake of comparison the figures are plotted with the same scale. A sketch of the position of points where the Δ are computed is plotted within each panel.

501
502
503   Figures 5(a) and (b) show the $\Delta\eta_{max}$ for two gauges located between the source and the coast and
504   beyond the trench respectively, while in Figure 5(c) the ΔD_{max} is shown for the first point on the
505   coast. Even though for the smallest modelled source, λ is more than 7 times larger than the
506   maximum sea-floor depth, and hence the SW limit is quite far to be violated (Abrahams et al.
507   2023), significant $\Delta_{\eta_{max}}$ with negative values down to -30% occurs, indicating that SW
508   systematically overestimates the NH wave amplitude during the coastward propagation (Figure
509   5a). For the slowest and smallest ruptures, the $\left|\Delta_{\eta_{max}}\right|$ is enhanced as an effect of short wavelength
510   oscillations affecting both the primary and the secondary waves. Such oscillations are due to
511   coupling of the dynamic evolution of the source with the instantaneous dissipative shock
512   introduced by the SW propagation (See wave evolution in left panels of Figure S12 in Supporting
513   Information).
514
515   For smaller ruptures, a similar SW overestimation is retrieved also in the open ocean propagation
516   beyond the trench, while a systematic underestimation emerges at intermediate and large source
517   sizes λ as shown in Figure 5(b).
518
519   However, such differences affect to a lesser extent the flow-depth maximum amplitude on the
520   coastal points with only few very slow simulations featuring a $\left|\Delta D_{max}\right|$ slightly larger than 0.1, as
521   evidenced in Figure 5(c) for the slowest ruptures.
522   Modelling NH and SW regimes with IS instead significantly reduces $\left|\Delta_{\eta_{max}}\right|$ offshore (Figures
523   S13a and b in Supporting Information) and $\left|\Delta D_{max}\right|$ on the coast (Figure S13c) for small source
524   size λ, while the SW underestimation for intermediate and large λ values, beyond the trench, is
525   characterized by similar $\Delta_{\eta_{max}}$. Despite in this condition the maximum amplitude metrics being
526   overall convergent, an interesting feature emerges following the waveform evolution with time for
527   the secondary waves. Indeed, when an instantaneous source is modelled, the NH propagation
528   generates high-frequency oscillations behind the primary wave possibly hampering the correct
529   modelling of secondary waves eventually generated by the dispersive propagation regime (Figure
530   S14 in Supporting Information). In other words, in case of instantaneous ruptures with strong
531   gradients, a singularity is generated on seafloor. The propagation of such a singularity generates a
532   train of secondary waves that propagates overlapping to the dispersive waves. Such effect has been
533   confirmed by laboratory experiment and convergence tests, performed with a refined grid and
534   modelling 5 and 7 non-hydrostatic layers.
535

536   4.2 Inundation and maximum run-up
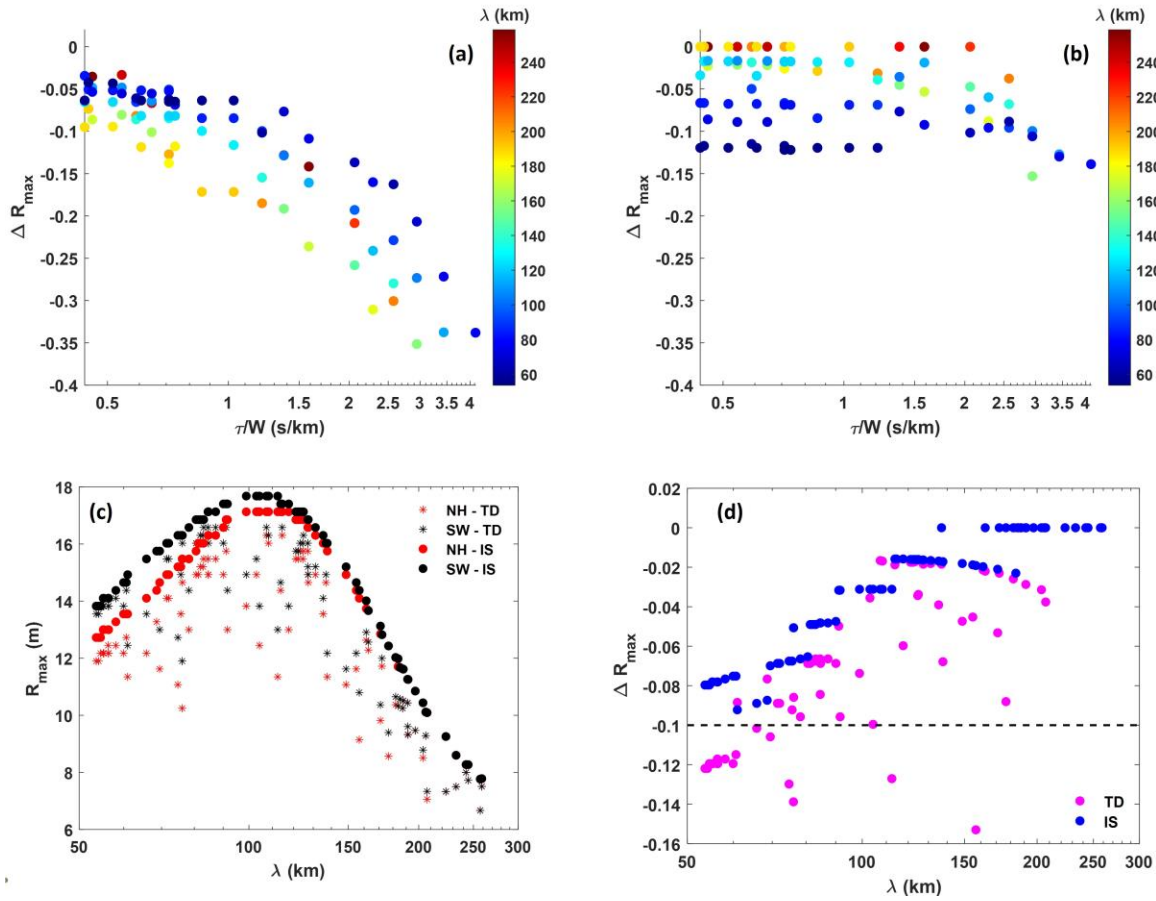
537

538   To address how the modelling approximations affect the inundation we used the maximum run-up
539   R_{max} and $\Delta_{R_{max}}$ as metrics. We performed similar comparisons as for the amplitude, first between
540   the TD-NH and IS-NH, and then between TD-SW and TD-NH. We show the results also for IS-
541   SW.
542   Figure 6(a) shows the ΔR_{max} for IS-NH taking TD-NH as a reference, as a function of τ/W and
543   λ. A trend similar to the one shown in Figure 4(a) is observed, with an increasing discrepancy for
544   slower and larger ruptures. However, the largest ruptures generate significantly smaller values of
545   both R_{max} and $\Delta_{R_{max}}$ as a consequence of the significant subsidence that completely prevents the
546   shoaling limiting the run-up. When the same comparison is performed between TD-NH and TD-
547   SW, we retrieved smaller discrepancies with maximum values of $\Delta_{R_{max}}$ around the 16% for the
548   smallest modelled sources (Figure 6b). A negligible contribution to the discrepancy is associated
549   to the parameter τ/W, which emerges only for very slow ruptures ($\tau/W > 3$ s/km)
550

551   The absolute R_{max} behavior for all the 81 simulations and for the 4 models is summarized in
552   Figure 6(c) evidencing a resonant character as a function of λ. The resonance is pretty perfect for
553   IS cases, with an optimal amplification for a narrow λ range, around 100-120 km. For TD sources,
554   both for SW and NH, R_{max} is also influenced by the source duration leading to a scattered R_{max}
555   pattern against λ still following the resonant trend. The λ value for which the resonance is observed
556   depends on the specific costal slope, as will be illustrated in Section 4.3.
557   Focusing on the discrepancies for SW simulations we also highlight that: i) the rupture size for
558   which the resonance is observed is independent of the propagation regime; ii) the overall SW
559   overestimation holds even when the more realistic TD-NH and TD-SW are compared. However,
560   in Figure 6(d), we observe that while with an IS the SW versus NH, ΔR_{max} is always less than
561   10%, it becomes larger with a TD source, with a maximum of about 16%. Looking at the time
562   evolution of inundation (Figure S15 in Supporting Information), we confirmed that the largest
563   ΔR_{max} emerging for small λ in TD simulations are actually due to the short-wavelength
564   oscillations (left panels of Figure S15 in Supporting Information). These oscillations are attenuated
565   for larger ruptures (Figure S15 of Supporting Information, right panels) and suppressed for IS
566   simulations (black dotted lines in Figure S14)
567   To summarize, as expected in realistic conditions for large subduction earthquakes, with $\lambda \gg H,$
568   the difference between NH and SW models are definitely less significant than the discrepancy
569   emerging between IS and TD simulations, at least in terms of wave maximum amplitude and
570   maximum run-up. However, the SW overestimation increases for very slow ruptures leading to
571    $|\Delta| \sim 20\%$ for the investigated metrics. In terms of waveform features, as seen, the use of either
572   a SW model for a TD source or a NH regime for instantaneous seafloor deformation causes short
573   wavelength oscillations affecting both the smaller oscillations behind the primary wave and,
574   sometimes, the inundation metrics, at least for $\lambda < \lambda_R$ with λ_R being the resonance wavelength
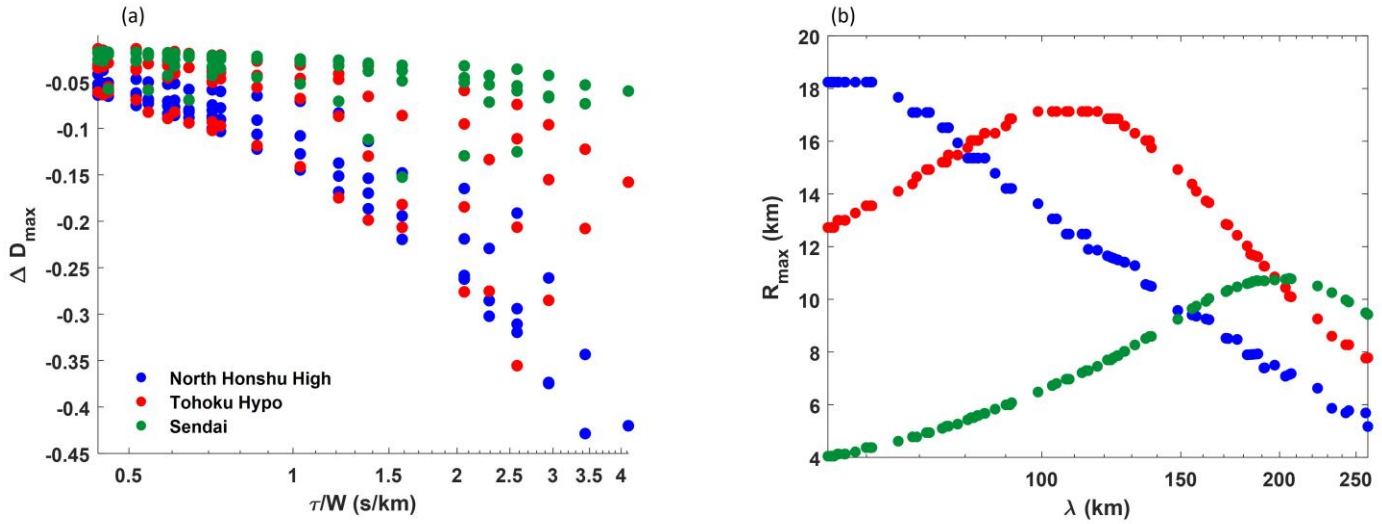575   described in Figure 6(c).
576

577

578

Figure 6: Maximum run-up R_{max} comparison between the four different models (TD-NH, IS-NH, TD-SW, IS-SW). (a) ΔR_{max} between TD-NH and IS-NH as a function of τ/W with color scale marking the source horizontal extension λ. (b) ΔR_{max} between TD-NH and TD-SW as a function of τ/W with color scale marking the source horizontal extension λ. For sake of comparison, the Figures in panels (a) and (b) are plotted with the same scale. (c) R_{max} on the coast as a function of λ for the four different models (d) ΔR_{max} as a function of λ with blue and magenta dots referring to IS-NH vs IS-SW and TD-NH Vs TD-SW comparison, respectively. The dashed line indicates that only for TD sources some simulations feature $|\Delta R_{max}| > 0.10$

588

589

590

591   4.3 Effect of bathymetry

To investigate the effect of different bathymetric conditions, particularly as far as the run-up resonance is concerned, we repeated the complete set of simulations for the other 5 simplified

594   topo-bathymetric profiles (Figure 1c). While the 6 different bathymetries are similar in the deep
595   part, they mostly differ in the slope at shallower depth in the vicinity of the coast and inland. Since
596   some bathymetric profiles are similar, in Figure 7(a) we only show the results for three of them.
597   The results shown so far were retrieved for the profile referred to as "Tohoku Hypo" (Figure 1c).
598   The southernmost profile referred to as "Sendai" is characterized by a significantly flatter slope,
599   while "North Honshu High" by a steeper slope in the vicinity of the coast. These three profiles are
600   interpreted as a proxy of the overall behavior in presence of intermediate, flat and steep topo-
601   bathymetric profiles, respectively.
602

Figure 7: Inundation metrics for different bathymetric geometry. (a) ΔD_{max} (TD-NH vs IS-NH) at the first point on the coast for the profiles referred to as "North Honshu High", "Tohoku Hypo" and "Sendai" respectively according to the map in Figure 1(c). (b) maximum run-up R_{max} (for IS-NH case) as a function of horizontal source extension λ for the 3 bathymetric profiles following the same legend of panel (a).

603
604   Figure 7(a) shows the $|\Delta D_{max}|$ between IS-NH and TD-NH source simulations at the first point
605   on the coast, for all the simulations and for the 3 different profiles. We retrieved for all the
606   bathymetries the double trend evidenced in Section 3.1 with larger discrepancy emerging not only
607   for slower ruptures but also for large size sources. However, a flatter bathymetry leads to smaller
608   $|\Delta D_{max}|$ implying that when a tsunami wave propagates towards more gentle depth variation an
609   instantaneous source would produce inundation scenarios more similar to time-dependent sources
610   as compared to steeper environments. Contemporarily, in a flatter environment, the inundation is
611   attenuated both in terms of flow-depth on the coast and maximum run-up with the size of resonance
612   that increases as the bathymetry slope decreases (see Figure 7b). For the sake of clarity, this latter
613   panel only shows the trends for the IS-NH case. However, we verified that, for all the bathymetries,
614   the rupture size for which the resonance occurs is independent of both the source treatment (IS or
615   TD) and the choice of propagation regime (NH or SW, compared with Figure 6c).
616   In conclusion, a gentler slope of the coast, as in the case of the flood plains in the area of Sendai-
617   Fukushima selects a longer wavelength component of tsunami waves, generating less intense
618   inundations in terms of both flow-depth on the coast and maximum run-up. Moreover, in a

619 Tohoku-like environment, like the one we have modelled in this study, the longer wavelengths are
620 more controlled by the deformation occurring very close to the hypocenter (Satake et al., 2013).
621 This contributes to reduce the discrepancy between IS and TD simulations for the flatter
622 bathymetric profiles.

5 Discussion

5.1 Comparison with real earthquakes and tsunamis

626 To understand in which cases time dependent and/or non-hydrostatic effects should be considered,
627 the 81 simulations performed for the "Tohoku Hypo" bathymetry (intermediate slope) are plotted
628 in Figure 8(a) as a function of their source slowness τ/W and size λ. They are classified depending
629 on whether the parameter ΔR_{max} (TD-NH vs IS-NH) is larger (red dots) or smaller (orange and
630 green dots) than 0.1, considering as acceptable a relative discrepancy smaller than 10%. The source
631 slowness and size are related to seismic parameters like the stress drop, the average rigidity and
632 hence the average depth of the source (Bilek & Lay, 1999; Geist & Bilek, 2001; Sallarès & Ranero,
633 2019). As expected, the slower the rupture the more time-dependent rupture modelling is needed.
634 The instantaneous approximation tends to fail when the characteristic tsunami propagation speed
635 at the source, on the order of $\sqrt{gH_{trench}}$ (with H_{trench} being the depth at the trench) is comparable
636 with the rupture velocity V_r, for which the quantity $(\tau/W)^{-1}$ acts as a proxy (e.g. see Abrahams et
637 al., 2023), as it occurs for the slowest ruptures considered here. However, beyond that, we found
638 that the ΔR_{max} (TD-NH vs IS-NH) also depends on the source size. Indeed, larger ruptures, for
639 which along-dip distance is comparable with trench-coast distance, more likely lead to inaccurate
640 solutions from approximated models. In these cases, the inundation is more controlled by what
641 happens at the source rather than by the propagation processes (e.g., the shoaling).
642 To provide modelers with tangible recommendations, we compared the parameters of the sources
643 presented in Figure 8(a) with those inferred for some subduction interface tsunamigenic
644 earthquakes . Their features are summarized in Table S3 of Supporting Information. We extracted
645 the duration τ, the width W and the dip angle from the teleseismic data inversions by Ye et al.
646 (2016), for all the events, including the Maule 2010 Mw 8.8 and the Tohoku-Oki 2011 Mw 9.1
647 earthquakes, with the exception of the 2004 Sumatra-Andaman earthquake, whose parameters are
648 taken   from   the   finite-fault   model   summary   released   by   USGS
649 (https://earthquake.usgs.gov/earthquakes/eventpage/official20041226005853450_30/finite-fault,
650 Banerjee et al. 2007). We computed a proxy of the source size along the dip as $\lambda = W \cdot \cos\delta$, with
651 δ being the dip angle (See Table S3 in Supporting Information). Such a comparison in Figure 8
652 has the goal of comparing the characteristic space and time scales of simulations with those of the
653 real events. However, single real events might be also affected by specific conditions related to
654 local geometry, shallow structure, bathymetry variation, and ratio between source size and trench-
655 coast distance as it happens for the Maule 2010 earthquake (Romano et al., 2020), which may
656 differ from the Tohoku-like setup used in our 1D simulations. Hence, this comparison should be
657 regarded as a general indication. Nonetheless, according to this comparison, some of the
658 megathrust events, characterized by relatively shallow slip and not too high stress-drop, such as
659 Maule 2010 and Tohoku 2011, are very close to the accuracy limit to use an instantaneous source,
660 while the 2004 Sumatra-Andaman event is well in the region where instantaneous source
661 modelling leads to inaccurate solutions and a time-dependent source should be used. The use of a
662 TD source implies, in turn, the necessity of a NH regime to avoid the spurious oscillations shown

663   in Figures S12 and S15 (in Supporting Information) and the consequent systematic SW
664   overestimation evidenced in Figures 6(c) and 6(d).
665   Conversely, large stress drop events (relatively rapid ones, sometimes referred to as "snappy"
666   earthquakes, see e.g. Ebeling & Okal, 2012; Okal et al., 2016) can be well modelled with an
667   instantaneous source. Finally, earthquakes featuring a small extension along the dip, might lead to
668   larger errors when modelled by an instantaneous source, if they are characterized by very slow
669   ruptures, like the tsunami earthquakes (small values of stress drop and rigidity). However, a direct
670   comparison between the findings of this study and tsunami earthquakes must be interpreted with
671   some prudence, since such events are characterized by a quite large along-strike extension as
672   compared to their width (Kanamori, 1971; Tanioka & Satake, 1996a; Tanioka & Seno, 2001). Such
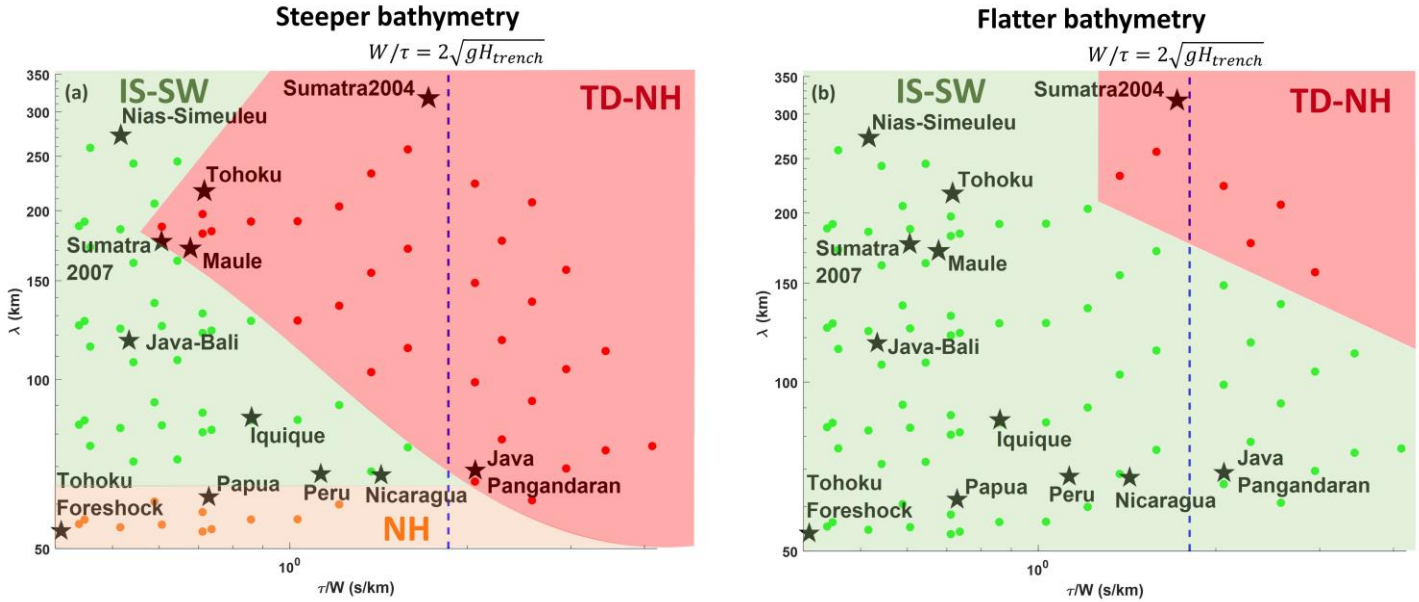673   a feature cannot be considered in the 1D model and will be the scope of future work.
674   Lastly, In Figure 8(a) the orange dots represent the simulations for which ΔR_{max} (TD-NH vs IS-
675   NH) < 0.1 while ΔR_{max} (TD-NH vs TD-SW) > 0.1. Such simulations are characterized by a small
676   source extension ($\lambda \sim 7 H_{trench}$) and, although they could be modelled through an IS description,
677   they require a NH modelling to avoid exceeding the imposed discrepancy tolerance. Within this
678   region we retrieve very short-sized interslab events like the 2009 Papua event or the Tohoku
679   foreshock of 2011, March 9th. In such a case, even if metrics like the maximum run-up are
680   accurately modelled through an IS approach, a TD source must be used to prevent the short
681   wavelength oscillations affecting the dispersive secondary waves (See red curves in Figure S14 in
682   Supporting Information). For the same reason, for faster events (e.g. deeper, larger stress drop
683   earthquakes for which $\sqrt{gH} \cdot \tau/W \ll 1$), that can be precisely simulated with an IS, the choice of
684   a SW modelling represents a preferable option (see green regions in Figure 8).

686   We have verified that ΔD_{max} or ΔR_{max} depend also on topographic features (see Figure 7a).
687   Figure 8(b) shows the same plot as Figure 8(a) with the ΔR_{max} values, but using the flatter
688   "Sendai" near-coast bathymetry and topography. As shown in Figure 7(a), the ΔD_{max} values on
689   the coast are smaller for flatter bathymetries and this leads to smaller Δ values also in terms of
690   maximum run-up. As a consequence, only very slow ($V_r < 0.5\ km/s$) and large ruptures (λ larger
691   than half trench-coast distance) yield inaccurate inundation modelling when an IS source is used
692   as a tsunami generation mechanism. Only the modelling of events similar to the giant 2004
693   Sumatra event would require a TD source. The differences highlighted between Figures 8(a) and
694   (b) are consistent with the results related to the 2011 Tohoku-Oki event, by Satake et al. (2013)
695   who showed how a time-dependent source modelling is required to accurately retrieve the
696   inundation features along the coast in front of the hypocenter of the event. Satake et al., (2013)
697   also showed that an instantaneous source was enough to model a realistic inundation in the
698   southern regions of Sendai and Fukushima. For flatter bathymetries, for which the shortest
699   wavelength sources generate negligible inundations, all the ΔR_{max} (TD-NH-vs TD-SW) values
700   are below the imposed tolerance of 0.1. For the sake of completeness, the results summarized in
701   Figure 8 are compared with the condition $W/\tau = 2\sqrt{gH_{trench}}$ that represents a proxy of the
702   instantaneous source limit (Abrahams et al., 2023). An equivalent horizontal line fixing as a
703   reference a SW limit $\lambda = 2 H_{trench}$ would be well below the shortest modelled source.

705   At least for a Tohoku-like up-dip rupture, using an instantaneous source always overestimates the
706   inundation on the coast as compared to the corresponding time dependent modelling. Therefore,
707   for some applications, the IS can be still used as a conservative approach, even though relatively
708   inaccurate, if a kinematic or a dynamic realistic description of the seismic source process is not
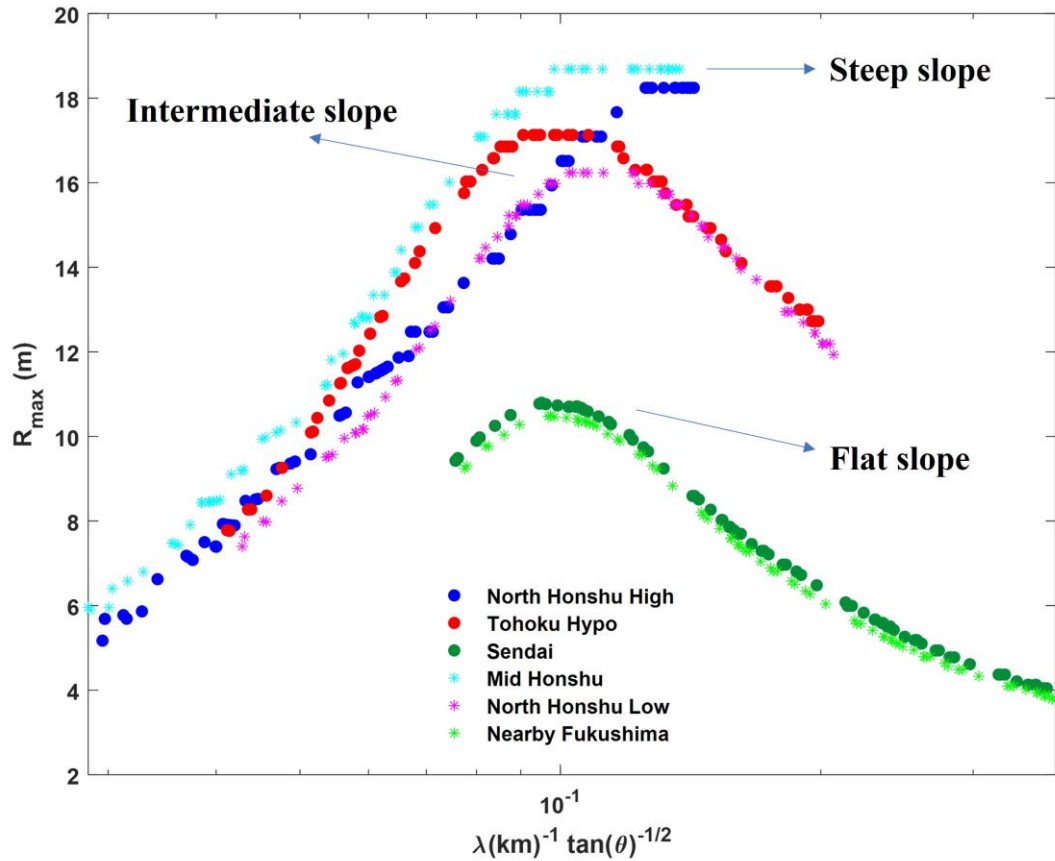
709 available. Nevertheless, we have also verified that for some simulations the maximum amplitude
710 of waves propagating towards the open ocean along the directive direction is underestimated by
711 the IS modelling. This might produce an underestimated inundation warning towards those islands
712 which are located along the up-dip direction, in the vicinity of the trench.
713

714 **Figure 8:** Summary of simulations that can be modelled with (green dots) and without (red and
715 orange dots) enough accuracy using simplified models in terms of maximum run-up R. In all
716 panels, each simulation is placed according to τ/W and λ with the green and red dots representing
717 $|\Delta R_{max}| \leq 0.1$ and $|\Delta R_{max}| > 0.1$ respectively when the comparison (TD-NH vs IS-NH) is
718 performed. Orange dots represent the simulations for which ΔR_{max} (TD-NH vs IS-NH) < 0.1
719 while ΔR_{max} (TD-NH vs TD-SW) > 0.1 The colored regions indicate the regions where different
720 models must be used. The blue dashed lines border the regions where the seismic rupture velocity
721 proxy W/τ is equal to 2 times the maximum tsunami velocity at the source $\sqrt{gH_{trench}}$. Panels (a)
722 and (b) refer to simulations performed on an intermediate slope ("Tohoku Hypo") and flat slope
723 bathymetry geometry ("Sendai"), respectively.

Figure 9: maximum run-up as a function of $1/\left(\lambda\sqrt{\tan\theta}\right)$ as suggested by the model of Stefanakis et al. (2012). As indicated by the arrows the blue dots and cyan stars refer to steeper slope geometry, the red dots and magenta stars to intermediate slope and the dark green dots and green stars to flatter slope bathymetry, respectively, as reported in the legend.

724

725   5.2 Resonance

726

727   Another important result concerns the size of the resonance observed in the computation of
728   maximum run-up and its connection to the geometry of bathymetric profiles. In this framework,
729   Stefanakis et al. (2012) have shown how a monochromatic source, with pulsation ω, generates
730   resonant waves whose maximum run-up on planar beaches depends on the incident wavelength
731   and beach slope (with larger run-ups associated with steeper slopes). They verified that for a fixed
732   beach length L the resonance is always retrieved at the same normalized pulsation $\omega' =$
733    $\omega/\sqrt{g\tan\theta/L}$, with g and θ being the gravity acceleration and the slope of the bathymetry (in the
734   vicinity of the beach and inland), respectively. To verify the consistency of the same model for our
735   application, we can replace ω with $1/\lambda$ since in the vicinity of the source the depth variation and

736 hence the propagation velocity are the same for all the bathymetries. Moreover, we can neglect the
737 effect of L because the beaches are always long enough to avoid backward reflections. Figure 9
738 shows the maximum run-up R_{max} for all the 81 IS-NH simulations and the 6 bathymetries, as a
739 function of the parameter $1/(\lambda\sqrt{\tan\theta})$, θ being the different slopes of the bathymetry in the
740 vicinity and on the coast. Although the sources modelled in this work are quite different as
741 compared to the simplified monochromatic source, with characteristic wavelength inherited by a
742 realistic parameterization of the seismic rupture, the resonant mechanism is preserved (compare
743 Figure 9 with Figure 7c) at least for instantaneous sources. When a TD source is implemented this
744 resonance symmetry is partially smeared since the maximum run-up is also controlled by the
745 seismic source duration (See Figure 6c), with slower ruptures leading to smaller inundation. This
746 latter result challenges the common assumption, for example, for tsunami earthquakes, that slow
747 ruptures are one of the reasons why larger than expected tsunami inundation for a given earthquake
748 magnitude is observed. Nevertheless, our modelling indicates that the inundation amplification
749 could still be due to larger slip occurring at shallower depths, where the surrounding medium is
750 weaker, and/or eventually to an unexpectedly large extension of the rupture along the strike
751 direction.
752
753
754

755   5.3 Limits of numerical modelling
756
757 Some of the choices made in terms of seismic source parameters deserve further discussion since
758 they can affect the investigated tsunami metrics. As an example, different values of the critical slip
759 weakening distance D_c or the possibility to consider the contribution of horizontal sea-floor
760 deformation (Tanioka & Satake, 1996b; Tanioka & Seno, 2001) to the tsunami initial condition
761 might modify the maximum amplitude of the source time history (see Figure 1b) and hence
762 generate different wave amplitudes, flow-depths, and maximum run-ups. Besides, as discussed in
763 section 3.3, we used a single slope to model the interface between the fault and the seafloor for all
764 the cases and this allowed us to perform several tsunami simulations from a single rupture dynamic
765 model. However, the use of a different and more realistic interface geometry is expected to slightly
766 change the wave amplitudes as an effect of the variable dip and its time history, even when ending
767 up with the same residual amplitude (See Figure S16a in Supporting Information). Nevertheless,
768 at least regarding the latter point, we verified for some of the performed simulations that the ranges
769 of ΔD_{max} on the coast and the $\Delta\eta_{max}$ offshore values (for TD-NH vs IS-NH comparison) are not
770 significantly affected by these initial source amplitude perturbations (See Figure S16 and its
771 caption in Supporting Information). Therefore, we can argue that the results presented in section
772 4 as well as the general interpretation presented in this section hold for most of the conditions that
773 simply affect the maximum amplitude of the waves triggered in the vicinity of the source.
774 We focused on megathrust earthquakes while tsunamis may arise also from other type of
775 mechanisms such as the outer-rise normal events for which time-dependent and non-hydrostatic
776 modelling might have a non-negligible effect as well (Baba et al., 2021). One should be cautious
777 to extend the findings of this study to those events and related tsunamis because they feature
778 different radiation fields and sea-floor deformation history and space scale.
779 Finally, more complex models, taking into account the solid-acoustic coupling at the elastic-fluid
780 interface (e.g. Ma, 2022), more sophisticated dynamic effects, like bi-material slip amplification

781   (e.g. Scala et al. 2017), off-fault damage dissipation (e.g. Wilson & Ma, 2021, Ma, 2023) and
782   realistic, short-sized bathymetry features as the ones shown within the insets of Figure 1(c), may
783   affect the results. All these physical complexities, even though well beyond the scope of this work,
784   deserve a deeper investigation possibly in a fully 3D coupled seismic-tsunami source model.

785   **6 Conclusions**
786

787   The main goal of this work is to understand when the accuracy needed to model the earthquake
788   source and tsunami generation can be achieved with the commonly adopted simplifications (e.g.
789   instantaneous source, shallow water) that reduce the computational cost. This is crucial for
790   applications like the PTHA (e.g., Grezio et al., 2017; Davies et al., 2018; Basili et al., 2021;
791   Behrens et al., 2021), where many scenarios need to be simulated, and tsunami early warning (e.g.,
792   Selva et al., 2021), where a short time-to-solution is needed. We measured the accuracy of the
793   solutions in terms of wave amplitude and inundation metrics (flow-depth and run-up) for a
794   Tohoku-like test-case using different topo-bathymetric morphologies. We systematically
795   compared the approximated results and the ones deriving from a more realistic representation of
796   the physical processes, accounting for a time-dependent earthquake-tsunami source and/or a multi-
797   layer non-hydrostatic tsunami modelling. We varied systematically the duration and the size of the
798   tsunami sources, using realistic ranges related to the corresponding seismic source and surrounding
799   medium parameters, in particular the stress drop and the rigidity around the fault plane.
800

801   The main results can be summarized as follows:
802   1. An instantaneous source leads to increasingly less accurate results as the velocity of the
803   seismic source decreases and becomes comparable with the characteristic velocity of
804   tsunami propagation, in turn proportional to the square root of the bathymetric depth.
805   However, within this framework, the size of the rupture also plays a fundamental role with
806   larger ruptures leading to less accurate solutions. The inundation metrics are
807   systematically overestimated by the instantaneous source approximation.
808   2. For what concerns the comparison between shallow water and non-hydrostatic, in realistic
809   conditions featuring an average bathymetric depth $H \ll \lambda$ (horizontal extension of the
810   source) the discrepancy for the maximum wave amplitudes and inundations are often not
811   significant. Even for very small ruptures the relative flow-depth and run-up overestimation
812   from SW-IS as compared to NH-IS are always smaller than the 10%. Nevertheless, when
813   we compare NH and SW in those conditions requiring TD source modelling, such
814   discrepancy increases up to ~20%. Thus, it is almost always recommended to use NH
815   modeling when dealing with time dependent seismic ruptures. In this frame, the common
816   use of multi sub-faults, activated at different instants, along with a SW propagation, might
817   lead to large overestimation.
818   3. All the results presented depend on the geometric characteristics of the topo/bathymetry
819   in the vicinity of the coast and inland. The differences between TD and IS inundation on
820   flatter bathymetric profiles (e.g., the ones characterizing the flood plains) are smaller than
821   those for steeper profiles. As a result, flooding on a flatter bathymetry could be modelled
822   with sufficient accuracy as an instantaneous source, as has been shown for some real
823   tsunamigenic events (Satake et al. 2013).
824   4. The maximum run-up features a resonant mechanism, that is an amplified R_{max} in
825   correspondence of a narrow range of the source size λ. The size of resonance was shown

826 to be inversely proportional to $\sqrt{\tan\theta}$ with θ being the topo-bathymetry slope in the
827 vicinity of the coastline.

828 5. Comparing all these results with real events, we found that megathrust and tsunami
829 earthquakes might require non-hydrostatic time-dependent modelling, in particular for
830 more pronounced variation of nearshore topo-bathymetry to prevent overestimation of
831 inundation intensity. Conversely, tsunami generated by deeper higher stress drop seismic
832 ruptures can be simulated through approximated IS-SW modelling, still preserving enough
833 accuracy in terms of propagating waves and inundation features.

834

840

841 **Open Research**

842 The whole simulated dataset is available at the following link:

843 https://zenodo.org/doi/10.5281/zenodo.10497579

844

845 All the figures were originally produced for this paper through the software MATLAB: version 2023b.

846 First accessed: September 2023. Academic license number: 40500131.

847

848 **References**

849 Abercrombie, R. E., Bannister, S., Ristau, J., & Doser, D. (2017). Variability of earthquake stress
850 drop in a subduction setting, the Hikurangi Margin, New Zealand. *Geophysical Journal*
851 *International*, *208*(1), 306–320. https://doi.org/10.1093/gji/ggw393

852 Abrahams, L. S., Krenz, L., Dunham, E. M., Gabriel, A.-A., & Saito, T. (2023). Comparison of
853 methods for coupled earthquake and tsunami modelling. *Geophysical Journal International*,
854 *234*(1), 404–426. https://doi.org/10.1093/gji/ggad053

855 Adsuara, J. E., Cordero-Carrión, I., Cerdá-Durán, P., & Aloy, M. A. (2016). Scheduled Relaxation
856 Jacobi method: Improvements and applications. Journal of Computational Physics, 321, 369–
857 413. https://doi.org/10.1016/j.jcp.2016.05.053

858 Audusse, E., Bristeau, M.-O., Perthame, B., & Sainte-Marie, J. (2011). A multilayer Saint-Venant
859 system with mass exchanges for shallow water flows. Derivation and numerical validation.
860 *ESAIM: Mathematical Modelling and Numerical Analysis*, *45*(1), 169–200.
861 https://doi.org/10.1051/m2an/2010036

Baba, T., Chikasada, N., Imai, K., Tanioka, Y., & Kodaira, S. (2021). Frequency dispersion amplifies tsunamis caused by outer-rise normal faults. *Scientific Reports*, *11*(1), 20064. https://doi.org/10.1038/s41598-021-99536-x

Babeyko, A., Lorito, S., Hernandez, F., Lauterjung, J., Løvholt, F., Rudloff, A., Sørensen, M., Androsov, A., Aniel-Quiroga, I., Armigliato, A., Baptista, M. A., Baglione, E., Basili, R., Behrens, J., Brizuela, B., Bruni, S., Cambaz, D., Cantavella Nadal, J., Carillho, F., … Yalciner, A. (2022). Towards the new Thematic Core Service Tsunami within the EPOS Research Infrastructure. *Annals of Geophysics*, *65*(2), DM215. https://doi.org/10.4401/ag-8762

Banerjee, P., Pollitz, F., Nagarajan, B., & Bürgmann, R. (2007). Coseismic Slip Distributions of the 26 December 2004 Sumatra–Andaman and 28 March 2005 Nias Earthquakes from <scp>gps</scp> Static Offsets. *Bulletin of the Seismological Society of America*, *97*(1A), S86–S102. https://doi.org/10.1785/0120050609

Basili, R., Brizuela, B., Herrero, A., Iqbal, S., Lorito, S., Maesano, F. E., Murphy, S., Perfetti, P., Romano, F., Scala, A., Selva, J., Taroni, M., Tiberti, M. M., Thio, H. K., Tonini, R., Volpe, M., Glimsdal, S., Harbitz, C. B., Løvholt, F., … Zaytsev, A. (2021). The Making of the NEAM Tsunami Hazard Model 2018 (NEAMTHM18). *Frontiers in Earth Science*, *8*. https://doi.org/10.3389/feart.2020.616594

Behrens, J., Løvholt, F., Jalayer, F., Lorito, S., Salgado-Gálvez, M. A., Sørensen, M., Abadie, S., Aguirre-Ayerbe, I., Aniel-Quiroga, I., Babeyko, A., Baiguera, M., Basili, R., Belliazzi, S., Grezio, A., Johnson, K., Murphy, S., Paris, R., Rafliana, I., De Risi, R., … Vyhmeister, E. (2021). Probabilistic Tsunami Hazard and Risk Analysis: A Review of Research Gaps. *Frontiers in Earth Science*, *9*. https://doi.org/10.3389/feart.2021.628772

Beji, S., & Battjes, J. A. (1994). Numerical simulation of nonlinear wave propagation over a bar. Coastal Engineering, 23(1–2), 1–16. https://doi.org/10.1016/0378-3839(94)90012-4

Bilek, S. L., & Lay, T. (1999). Rigidity variations with depth along interplate megathrust faults in subduction zones. *Nature*, *400*(6743), 443–446. https://doi.org/10.1038/22739

Bilek, S. L., Rotman, H. M. M., & Phillips, W. S. (2016). Low stress drop earthquakes in the rupture zone of the 1992 Nicaragua tsunami earthquake. *Geophysical Research Letters*, *43*(19). https://doi.org/10.1002/2016GL070409

Bonaventura, L., Fernández-Nieto, E. D., Garres-Díaz, J., & Narbona-Reina, G. (2018). Multilayer shallow water models with locally variable number of layers and semi-implicit time discretization. *Journal of Computational Physics*, *364*, 209–234. https://doi.org/10.1016/j.jcp.2018.03.017

Brocchini, M., & Peregrine, D. H. (1996). Integral flow properties of the swash zone and averaging. *Journal of Fluid Mechanics*, *317*, 241–273. https://doi.org/10.1017/S0022112096000742

Burridge, R. (1973). Admissible Speeds for Plane-Strain Self-Similar Shear Cracks with Friction but Lacking Cohesion. *Geophysical Journal International*, *35*(4), 439–455. https://doi.org/10.1111/j.1365-246X.1973.tb00608.x

Castro Díaz, M. J., & Fernández-Nieto, E. (2012). A Class of Computationally Fast First Order Finite Volume Solvers: PVM Methods. SIAM Journal on Scientific Computing, 34(4), A2173–A2196. https://doi.org/10.1137/100795280

Casulli, V. (1999). A semi-implicit finite difference method for non-hydrostatic, free-surface flows. *International Journal for Numerical Methods in Fluids*, *30*(4), 425–440. https://doi.org/10.1002/(SICI)1097-0363(19990630)30:4<425::AID-FLD847>3.0.CO;2-D

Chazel, F., Lannes, D., & Marche, F. (2011). Numerical Simulation of Strongly Nonlinear and Dispersive Waves Using a Green–Naghdi Model. Journal of Scientific Computing, 48(1–3), 105–116. https://doi.org/10.1007/s10915-010-9395-9

Chorin, A. J. (1968). Numerical Solution of the Navier-Stokes Equations. Mathematics of Computation, 22(104), 745. https://doi.org/10.2307/2004575

Davies, G., & Griffin, J. (2020). Sensitivity of Probabilistic Tsunami Hazard Assessment to Far-Field Earthquake Slip Complexity and Rigidity Depth-Dependence: Case Study of Australia. *Pure and Applied Geophysics*, *177*(3), 1521–1548. https://doi.org/10.1007/s00024-019-02299-w

Davies, G., Griffin, J., Løvholt, F., Glimsdal, S., Harbitz, C., Thio, H. K., Lorito, S., Basili, R., Selva, J., Geist, E., & Baptista, M. A. (2018). A global probabilistic tsunami hazard assessment from earthquake sources. *Geological Society, London, Special Publications*, *456*(1), 219–244. https://doi.org/10.1144/SP456.5

Davies, G., Weber, R., Wilson, K., & Cummins, P. (2022). From offshore to onshore probabilistic tsunami hazard assessment via efficient Monte Carlo sampling. *Geophysical Journal International*, *230*(3), 1630–1651. https://doi.org/10.1093/gji/ggac140

Dingemans, M. W. (1994). MAST PROJECT 1: WAVES G8-M Comparison of computations with Boussinesq-like models and laboratory measurements.

Ebeling, C. W., & Okal, E. A. (2012). An extension of the E/M0 tsunami earthquake discriminant Θ to regional distances. *Geophysical Journal International*, *190*(3), 1640–1656. https://doi.org/10.1111/j.1365-246X.2012.05566.x

Ehara, A., Salmanidou, D. M., Heidarzadeh, M., & Guillas, S. (2023). Multi-level emulation of tsunami simulations over Cilacap, South Java, Indonesia. *Computational Geosciences*, *27*(1), 127–142. https://doi.org/10.1007/s10596-022-10183-1

Escalante, C., Fernández-Nieto, E. D., Garres-Díaz, J., & Mangeney, A. (2023). Multilayer Shallow Model for Dry Granular Flows with a Weakly Non-hydrostatic Pressure. *Journal of Scientific Computing*, *96*(3), 88. https://doi.org/10.1007/s10915-023-02299-y

Escalante, C., Fernández-Nieto, E. D., Garres-Díaz, J., Morales de Luna, T., & Penel, Y. (2023). Non-hydrostatic layer-averaged approximation of Euler system with enhanced dispersion properties. *Computational and Applied Mathematics*, *42*(4), 177. https://doi.org/10.1007/s40314-023-02309-7

Escalante, C., Fernández-Nieto, E. D., Morales de Luna, T., & Castro, M. J. (2019). An Efficient Two-Layer Non-hydrostatic Approach for Dispersive Water Waves. *Journal of Scientific Computing*, *79*(1), 273–320. https://doi.org/10.1007/s10915-018-0849-9

Escalante, C., Morales de Luna, T., & Castro, M. J. (2018). Non-hydrostatic pressure shallow flows: GPU implementation using finite volume and finite difference scheme. *Applied Mathematics and Computation*, *338*, 631–659. https://doi.org/10.1016/j.amc.2018.06.035

Fernández-Nieto, E. D., Koné, E. H., & Chacón Rebollo, T. (2014). A Multilayer Method for the Hydrostatic Navier-Stokes Equations: A Particular Weak Solution. *Journal of Scientific Computing*, *60*(2), 408–437. https://doi.org/10.1007/s10915-013-9802-0

Fernández-Nieto, E. D., Parisot, M., Penel, Y., & Sainte-Marie, J. (2018). A hierarchy of dispersive layer-averaged approximations of Euler equations for free surface flows. *Communications in Mathematical Sciences*, *16*(5), 1169–1202. https://doi.org/10.4310/CMS.2018.v16.n5.a1

Festa, G., & Vilotte, J.-P. (2005). The Newmark scheme as velocity-stress time-staggering: an efficient PML implementation for spectral element simulations of elastodynamics.

Geophysical Journal International, *161*(3), 789–812. https://doi.org/10.1111/j.1365-246X.2005.02601.x

Folesky, J., Kummerow, J., & Shapiro, S. A. (2021). Stress Drop Variations in the Region of the 2014 M_W 8.1 Iquique Earthquake, Northern Chile. *Journal of Geophysical Research: Solid Earth*, *126*(4). https://doi.org/10.1029/2020JB020112

Gailler, A., Hébert, H., Schindelé, F., & Reymond, D. (2018). Coastal Amplification Laws for the French Tsunami Warning Center: Numerical Modeling and Fast Estimate of Tsunami Wave Heights Along the French Riviera. *Pure and Applied Geophysics*, *175*(4), 1429–1444. https://doi.org/10.1007/s00024-017-1713-9

Geist, E. L., & Bilek, S. L. (2001). Effect of depth-dependent shear modulus on tsunami generation along subduction zones. *Geophysical Research Letters*, *28*(7), 1315–1318. https://doi.org/10.1029/2000GL012385

Gibbons, S. J., Lorito, S., Macías, J., Løvholt, F., Selva, J., Volpe, M., Sánchez-Linares, C., Babeyko, A., Brizuela, B., Cirella, A., Castro, M. J., de la Asunción, M., Lanucara, P., Glimsdal, S., Lorenzino, M. C., Nazaria, M., Pizzimenti, L., Romano, F., Scala, A., … Vöge, M. (2020). Probabilistic Tsunami Hazard Analysis: High Performance Computing for Massive Scale Inundation Simulations. *Frontiers in Earth Science*, *8*. https://doi.org/10.3389/feart.2020.591549

Glimsdal, S., Løvholt, F., Harbitz, C. B., Romano, F., Lorito, S., Orefice, S., Brizuela, B., Selva, J., Hoechner, A., Volpe, M., Babeyko, A., Tonini, R., Wronna, M., & Omira, R. (2019). A New Approximate Method for Quantifying Tsunami Maximum Inundation Height Probability. *Pure and Applied Geophysics*, *176*(7), 3227–3246. https://doi.org/10.1007/s00024-019-02091-w

Gopinathan, D., Heidarzadeh, M., & Guillas, S. (2021). Probabilistic quantification of tsunami current hazard using statistical emulation. *Proceedings of the Royal Society A: Mathematical, Physical and Engineering Sciences*, *477*(2250). https://doi.org/10.1098/rspa.2021.0180

Grezio, A., Babeyko, A., Baptista, M. A., Behrens, J., Costa, A., Davies, G., Geist, E. L., Glimsdal, S., González, F. I., Griffin, J., Harbitz, C. B., LeVeque, R. J., Lorito, S., Løvholt, F., Omira, R., Mueller, C., Paris, R., Parsons, T., Polet, J., … Thio, H. K. (2017). Probabilistic Tsunami Hazard Analysis: Multiple Sources and Global Applications. *Reviews of Geophysics*, *55*(4), 1158–1198. https://doi.org/10.1002/2017RG000579

Hayes, G. P., Moore, G. L., Portner, D. E., Hearne, M., Flamme, H., Furtney, M., & Smoczyk, G. M. (2018). Slab2, a comprehensive subduction zone geometry model. *Science*, *362*(6410), 58–61. https://doi.org/10.1126/science.aat4723

Huang, Y., Meng, L., & Ampuero, J.-P. (2012). A dynamic model of the frequency-dependent rupture process of the 2011 Tohoku-Oki earthquake. *Earth, Planets and Space*, *64*(12), 1061–1066. https://doi.org/10.5047/eps.2012.05.011

Ida, Y. (1972). Cohesive force across the tip of a longitudinal-shear crack and Griffith's specific surface energy. *Journal of Geophysical Research*, *77*(20), 3796–3805. https://doi.org/10.1029/JB077i020p03796

Kajiura, K. (1963). The leading wave of a tsunami. *Bulletin of Earthquake Research Institute, University of Tokyo*, *41*, 535–571.

Kanamori, H. (1971). Seismological evidence for a lithospheric normal faulting — the Sanriku earthquake of 1933. *Physics of the Earth and Planetary Interiors*, *4*(4), 289–300. https://doi.org/10.1016/0031-9201(71)90013-6

998 Kanamori, H., & Brodsky, E. E. (2004). The physics of earthquakes. *Reports on Progress in*
999   *Physics*, *67*(8), 1429–1496. https://doi.org/10.1088/0034-4885/67/8/R03

1000 Kazolea, M., & Delis, A. I. (2013). A well-balanced shock-capturing hybrid finite volume–finite
1001   difference numerical scheme for extended 1D Boussinesq models. Applied Numerical
1002   Mathematics, 67, 167–186. https://doi.org/10.1016/j.apnum.2011.07.003

1003 Komatitsch, D., & Vilotte, J.-P. (1998). The spectral element method: An efficient tool to simulate
1004   the seismic response of 2D and 3D geological structures. *Bulletin of the Seismological Society*
1005   *of America*, *88*(2), 368–392. https://doi.org/10.1785/BSSA0880020368

1006 Kozdon, J. E., & Dunham, E. M. (2013). Rupture to the Trench: Dynamic Rupture Simulations of
1007   the 11 March 2011 Tohoku Earthquake. *Bulletin of the Seismological Society of America*,
1008   *103*(2B), 1275–1289. https://doi.org/10.1785/0120120136

1009 LeVeque, R. J., Waagan, K., González, F. I., Rim, D., & Lin, G. (2016). Generating Random
1010   Earthquake Events for Probabilistic Tsunami Hazard Assessment. *Pure and Applied*
1011   *Geophysics*, *173*(12), 3671–3692. https://doi.org/10.1007/s00024-016-1357-1

1012 Li, L., Lay, T., Cheung, K. F., & Ye, L. (2016). Joint modeling of teleseismic and tsunami wave
1013   observations to constrain the 16 September 2015 Illapel, Chile, M_w 8.3 earthquake rupture
1014   process. *Geophysical Research Letters*, *43*(9), 4303–4312.
1015   https://doi.org/10.1002/2016GL068674

1016 Lotto, G. C., & Dunham, E. M. (2015). High-order finite difference modeling of tsunami
1017   generation in a compressible ocean from offshore earthquakes. *Computational Geosciences*,
1018   *19*(2), 327–340. https://doi.org/10.1007/s10596-015-9472-0

1019 Lotto, G. C., Jeppson, T. N., & Dunham, E. M. (2019). Fully Coupled Simulations of Megathrust
1020   Earthquakes and Tsunamis in the Japan Trench, Nankai Trough, and Cascadia Subduction
1021   Zone. *Pure and Applied Geophysics*, *176*(9), 4009–4041. https://doi.org/10.1007/s00024-
1022   018-1990-y

1023 Ludwig, W. J., Nafe, J. E., & Drake, C. L. (1970). Seismic refraction New York: Wiley-
1024   Interscience. *The Sea, Edited by Maxwell, A. E.*, *4*(1), 53–84.

1025 Ma, G., Shi, F., & Kirby, J. T. (2012). Shock-capturing non-hydrostatic model for fully dispersive
1026   surface wave processes. *Ocean Modelling*, *43–44*, 22–35.
1027   https://doi.org/10.1016/j.ocemod.2011.12.002

1028 Ma, S. (2022). Dynamic off-fault failure and tsunamigenesis at strike-slip restraining bends: Fully-
1029   coupled models of dynamic rupture, ocean acoustic waves, and tsunami in a shallow bay.
1030   *Tectonophysics*, *838*, 229496. https://doi.org/10.1016/j.tecto.2022.229496

1031 Ma, S. (2023). Wedge plasticity and a minimalist dynamic rupture model for the 2011 MW 9.1
1032   Tohoku-Oki earthquake and tsunami. *Tectonophysics*, *869*, 230146.
1033   https://doi.org/10.1016/j.tecto.2023.230146

1034 Macías, J., Escalante, C., & Castro, M. J. (2021a). Multilayer-HySEA model validation for
1035   landslide-generated tsunamis – Part 1: Rigid slides. *Natural Hazards and Earth System*
1036   *Sciences*, *21*(2), 775–789. https://doi.org/10.5194/nhess-21-775-2021

1037 Macías, J., Escalante, C., & Castro, M. J. (2021b). Multilayer-HySEA model validation for
1038   landslide-generated tsunamis – Part 2: Granular slides. *Natural Hazards and Earth System*
1039   *Sciences*, *21*(2), 791–805. https://doi.org/10.5194/nhess-21-791-2021

1040 Makinoshima, F., Oishi, Y., Yamazaki, T., Furumura, T., & Imamura, F. (2021). Early forecasting
1041   of tsunami inundation from tsunami and geodetic observation data with convolutional neural
1042   networks. *Nature Communications*, *12*(1), 2253. https://doi.org/10.1038/s41467-021-22348-
1043   0

Meade, B. J. (2007). Algorithms for the calculation of exact displacements, strains, and stresses for triangular dislocation elements in a uniform elastic half space. *Computers & Geosciences*, *33*(8), 1064–1075. https://doi.org/10.1016/j.cageo.2006.12.003

Miyake, H., Koketsu, K., & Furumura, T. (2008). *SOURCE MODELING OF SUBDUCTION-ZONE EARTHQUAKES AND LONG-PERIOD GROUND MOTION VALIDATION IN THE TOKYO METROPOLITAN AREA*.

Murphy, S., Di Toro, G., Romano, F., Scala, A., Lorito, S., Spagnuolo, E., Aretusini, S., Festa, G., Piatanesi, A., & Nielsen, S. (2018). Tsunamigenic earthquake simulations using experimentally derived friction laws. *Earth and Planetary Science Letters*, *486*, 155–165. https://doi.org/10.1016/j.epsl.2018.01.011

Murphy, S., Scala, A., Herrero, A., Lorito, S., Festa, G., Trasatti, E., Tonini, R., Romano, F., Molinari, I., & Nielsen, S. (2016). Shallow slip amplification and enhanced tsunami hazard unravelled by dynamic simulations of mega-thrust earthquakes. *Scientific Reports*, *6*(1), 35007. https://doi.org/10.1038/srep35007

Nakano, M., Murphy, S., Agata, R., Igarashi, Y., Okada, M., & Hori, T. (2020). Self-similar stochastic slip distributions on a non-planar fault for tsunami scenarios for megathrust earthquakes. *Progress in Earth and Planetary Science*, *7*(1), 45. https://doi.org/10.1186/s40645-020-00360-0

Oglesby, D. D., Archuleta, R. J., & Nielsen, S. B. (2000). Dynamics of dip-slip faulting: Explorations in two dimensions. *Journal of Geophysical Research: Solid Earth*, *105*(B6), 13643–13653. https://doi.org/10.1029/2000JB900055

Okada, Y. (1985). Surface deformation due to shear and tensile faults in a half-space. *Bulletin of the Seismological Society of America*, *75*(4), 1135–1154. https://doi.org/10.1785/BSSA0750041135

Okal, E. A., Kirby, S. H., & Kalligeris, N. (2016). The Showa Sanriku earthquake of 1933 March 2: a global seismological reassessment. *Geophysical Journal International*, *206*(3), 1492–1514. https://doi.org/10.1093/gji/ggw206

Ricchiuto, M., & Filippini, A. G. (2014). Upwind residual discretization of enhanced Boussinesq equations for wave propagation over complex bathymetries. Journal of Computational Physics, 271, 306–341. https://doi.org/10.1016/j.jcp.2013.12.048

Roeber, V., Cheung, K. F., & Kobayashi, M. H. (2010). Shock-capturing Boussinesq-type model for nearshore wave processes. *Coastal Engineering*, *57*(4), 407–423. https://doi.org/10.1016/j.coastaleng.2009.11.007

Romano, F., Gusman, A. R., Power, W., Piatanesi, A., Volpe, M., Scala, A., & Lorito, S. (2021). Tsunami Source of the 2021 M_W 8.1 Raoul Island Earthquake From DART and Tide-Gauge Data Inversion. *Geophysical Research Letters*, *48*(17). https://doi.org/10.1029/2021GL094449

Romano, F., Lorito, S., Lay, T., Piatanesi, A., Volpe, M., Murphy, S., & Tonini, R. (2020). Benchmarking the Optimal Time Alignment of Tsunami Waveforms in Nonlinear Joint Inversions for the Mw 8.8 2010 Maule (Chile) Earthquake. *Frontiers in Earth Science*, *8*. https://doi.org/10.3389/feart.2020.585429

Saito, T., Baba, T., Inazu, D., Takemura, S., & Fukuyama, E. (2019). Synthesizing sea surface height change including seismic waves and tsunami using a dynamic rupture scenario of anticipated Nankai trough earthquakes. *Tectonophysics*, *769*, 228166. https://doi.org/10.1016/j.tecto.2019.228166

Sallarès, V., & Ranero, C. R. (2019). Upper-plate rigidity determines depth-varying rupture behaviour of megathrust earthquakes. *Nature*, *576*(7785), 96–101. https://doi.org/10.1038/s41586-019-1784-0

Satake, K., Fujii, Y., Harada, T., & Namegaya, Y. (2013). Time and Space Distribution of Coseismic Slip of the 2011 Tohoku Earthquake as Inferred from Tsunami Waveform Data. *Bulletin of the Seismological Society of America*, *103*(2B), 1473–1492. https://doi.org/10.1785/0120120122

Scala, A., Festa, G., Vilotte, J. -P., Lorito, S., & Romano, F. (2019). Wave Interaction of Reverse-Fault Rupture With Free Surface: Numerical Analysis of the Dynamic Effects and Fault Opening Induced by Symmetry Breaking. *Journal of Geophysical Research: Solid Earth*, *124*(2), 1743–1758. https://doi.org/10.1029/2018JB016512

Scala, A., Festa, G., & Vilotte, J.-P. (2017). Rupture dynamics along bimaterial interfaces: a parametric study of the shear-normal traction coupling. *Geophysical Journal International*, ggw489. https://doi.org/10.1093/gji/ggw489

Scala, A., Lorito, S., Romano, F., Murphy, S., Selva, J., Basili, R., Babeyko, A., Herrero, A., Hoechner, A., Løvholt, F., Maesano, F. E., Perfetti, P., Tiberti, M. M., Tonini, R., Volpe, M., Davies, G., Festa, G., Power, W., Piatanesi, A., & Cirella, A. (2020). Effect of Shallow Slip Amplification Uncertainty on Probabilistic Tsunami Hazard Analysis in Subduction Zones: Use of Long-Term Balanced Stochastic Slip Models. *Pure and Applied Geophysics*, *177*(3), 1497–1520. https://doi.org/10.1007/s00024-019-02260-x

Scala, A. (2024). Dataset repository for paper "On the relation between seismic source dynamics, tsunami generation and propagation, and numerical modelling complexity for large earthquakes in subduction zones" [Data set]. Zenodo. https://doi.org/10.5281/zenodo.10497580

Selva, J., Lorito, S., Volpe, M., Romano, F., Tonini, R., Perfetti, P., Bernardi, F., Taroni, M., Scala, A., Babeyko, A., Løvholt, F., Gibbons, S. J., Macías, J., Castro, M. J., González-Vida, J. M., Sánchez-Linares, C., Bayraktar, H. B., Basili, R., Maesano, F. E., … Amato, A. (2021). Probabilistic tsunami forecasting for early warning. *Nature Communications*, *12*(1), 5677. https://doi.org/10.1038/s41467-021-25815-w

Sepúlveda, I., Liu, P. L. -F., Grigoriu, M., & Pritchard, M. (2017). Tsunami hazard assessments with consideration of uncertain earthquake slip distribution and location. *Journal of Geophysical Research: Solid Earth*, *122*(9), 7252–7271. https://doi.org/10.1002/2017JB014430

Skarlatoudis, A. A., Somerville, P. G., & Thio, H. K. (2016). Source-Scaling Relations of Interface Subduction Earthquakes for Strong Ground Motion and Tsunami Simulation. *Bulletin of the Seismological Society of America*, *106*(4), 1652–1662. https://doi.org/10.1785/0120150320

Souty, V., & Gailler, A. (2021). Fast High-Resolution S-PTHA Along the Western Mediterranean Sea Coastlines. Application to the Bay of Cannes. *Frontiers in Earth Science*, *9*. https://doi.org/10.3389/feart.2021.765610

Stefanakis, T., Dias, F., & Dutykh, D. (2012). Resonant Long-Wave Run-Up On A Plane Beach. *Proceedings of the 22nd (2012) International Offshore and Polar Engineering Conference*, 116–121. https://hal.science/hal-00728747

Stoker J. J. (1992). *Water Waves: The Mathematical Theory with Applications*. Wiley Classic Library.

Strasser, F. O., Arango, M. C., & Bommer, J. J. (2010). Scaling of the Source Dimensions of Interface and Intraslab Subduction-zone Earthquakes with Moment Magnitude. *Seismological Research Letters*, *81*(6), 941–950. https://doi.org/10.1785/gssrl.81.6.941

Sugawara, D. (2021). Numerical modeling of tsunami: advances and future challenges after the 2011 Tohoku earthquake and tsunami. *Earth-Science Reviews*, *214*, 103498. https://doi.org/10.1016/j.earscirev.2020.103498

Takahashi, N., Kodaira, S., Tsuru, T., Park, J.-O., Kaneda, Y., Suyehiro, K., Kinoshita, H., Abe, S., Nishino, M., & Hino, R. (2004). Seismic structure and seismogenesis off Sanriku region, northeastern Japan. *Geophysical Journal International*, *159*(1), 129–145. https://doi.org/10.1111/j.1365-246X.2004.02350.x

Tanioka, Y., & Satake, K. (1996a). Fault parameters of the 1896 Sanriku Tsunami Earthquake estimated from Tsunami Numerical Modeling. *Geophysical Research Letters*, *23*(13), 1549–1552. https://doi.org/10.1029/96GL01479

Tanioka, Y., & Satake, K. (1996b). Tsunami generation by horizontal displacement of ocean bottom. *Geophysical Research Letters*, *23*(8), 861–864. https://doi.org/10.1029/96GL00736

Tanioka, Y., & Seno, T. (2001). Sediment effect on tsunami generation of the 1896 Sanriku Tsunami Earthquake. *Geophysical Research Letters*, *28*(17), 3389–3392. https://doi.org/10.1029/2001GL013149

Titov, V. V., & Synolakis, C. E. (1995). Modeling of Breaking and Nonbreaking Long-Wave Evolution and Runup Using VTCS-2. Journal of Waterway, Port, Coastal, and Ocean Engineering, 121(6), 308–316. https://doi.org/10.1061/(ASCE)0733-950X(1995)121:6(308)

Tonini, R., Basili, R., Maesano, F. E., Tiberti, M. M., Lorito, S., Romano, F., Scala, A., & Volpe, M. (2020). Importance of earthquake rupture geometry on tsunami modelling: the Calabrian Arc subduction interface (Italy) case study. *Geophysical Journal International*, *223*(3), 1805–1819. https://doi.org/10.1093/gji/ggaa409

Uenishi, K., & Rice, J. R. (2003). Universal nucleation length for slip-weakening rupture instability under nonuniform fault loading. *Journal of Geophysical Research: Solid Earth*, *108*(B1). https://doi.org/10.1029/2001JB001681

Venkataraman, A., & Kanamori, H. (2004). Observational constraints on the fracture energy of subduction zone earthquakes. *Journal of Geophysical Research: Solid Earth*, *109*(B5). https://doi.org/10.1029/2003JB002549

Williamson, A. L., Rim, D., Adams, L. M., LeVeque, R. J., Melgar, D., & González, F. I. (2020). A Source Clustering Approach for Efficient Inundation Modeling and Regional Scale Probabilistic Tsunami Hazard Assessment. *Frontiers in Earth Science*, *8*. https://doi.org/10.3389/feart.2020.591663

Wilson, A., & Ma, S. (2021). Wedge Plasticity and Fully Coupled Simulations of Dynamic Rupture and Tsunami in the Cascadia Subduction Zone. *Journal of Geophysical Research: Solid Earth*, *126*(7). https://doi.org/10.1029/2020JB021627

Yamada, N., & Iwata, T. (2005). Long-period ground motion simulation in the Kinki area during the MJ 7.1 foreshock of the 2004 off the Kii peninsula earthquakes. *Earth, Planets and Space*, *57*(3), 197–202. https://doi.org/10.1186/BF03351815

Ye, L., Lay, T., Kanamori, H., & Rivera, L. (2016). Rupture characteristics of major and great ($M_w \geq 7.0$) megathrust earthquakes from 1990 to 2015: 1. Source parameter scaling relationships. *Journal of Geophysical Research: Solid Earth*, *121*(2), 826–844. https://doi.org/10.1002/2015JB012426

1178   Yoshimoto, M., & Yamanaka, Y. (2014). Teleseismic inversion of the 2004 Sumatra-Andaman
1179   earthquake rupture process using complete Green's functions. *Earth, Planets and Space*,
1180   *66*(1), 152. https://doi.org/10.1186/s40623-014-0152-4

1181

1182

1183